UCLouvain

epl

École polytechnique de Louvain

Development of an immersed material response code for thermal protection system

Author: **Florent Beauvois**
Supervisors: **Philippe Chatelain, Pierre Schrooyen**
Readers: **Francesco Contino, Hervé Jeanmart**
Academic year 2021–2022
Master [120] in Electro-mechanical Engineering

Acknowledgements

Avant de commencer ce rapport, je tiens à remercier les personnes qui m'ont aidé, soutenu et encouragé durant cette épreuve difficile.

Merci tout d'abord à mes promoteurs, et particulièrement Pierre Schrooyen, sans qui ce mémoire n'aurait pas vu le jour. Il a été présent chaque semaine pour répondre à mes questions et partager ses connaissances sur: la physique de la rentrée atmosphérique, les boucliers thermiques, l'implémentation d'Argo et ses innombrables lignes de code, etc. Je le remercie pour sa bienveillance et sa patience, notamment en décembre, lorsqu'il m'a aidé pendant plusieurs heures à installer et compiler Argo sur ma machine virtuelle. De plus, quand les simulations crashaient, il m'a toujours donné de bons conseils pour m'aider à trouver une solution.

Je remercie aussi les membres du jury qui ont montré de l'intérêt pour mon mémoire et qui ont accepté de lire ce document.

J'exprime également toute ma gratitude envers ma famille qui m'épaule depuis toujours et qui m'a soutenu durant ce mémoire. Pour l'anecdote, merci à mes parents de m'avoir prêté leur ordinateur pour l'écriture de ce rapport (car le mien faisait tellement de bruit pendant les simulations qu'il était difficile de se concentrer).

Merci aussi à mes amis qui m'ont encouragé dans les moments difficiles. En particulier, les anciens du groupe CBS&Kalié (mon groupe de projet en bac 1) qui m'ont aidé à décompresser autour d'une bière ou d'une partie de bowling.

Enfin, je tiens à remercier Sarah et ses parents pour leur soutient. Durant cette année, elle a toujours exprimé de l'intérêt pour mon mémoire et elle a été ma source de motivation principale. Sa présence m'a aidé à garder le sourire et ses encouragements m'ont permis de ne pas baisser les bras.

Contents

Nomenclature

Abbreviations

CFD Computational Fluid Dynamics

DGM Discontinuous Galerkin Method

ESA European Space Agency

FIRE Flight Investigation of Re-Entry

ISS International Space Station

IXV Intermediate eXperimental Vehicle

MSL Mars Science Laboratory

NASA National Aeronautics and Space Administration

PICA Phenolic Impregnated Carbon Ablator

SEM Scanning Electron Microscope

TACOT Theoretical Ablative Composite for Open Testing

TPS Thermal Protection System

VOF Volume Of Fluid

Alpha numeric symbols

A_s	Arrhenius law pre-exponential factor	[-]
B'	Dimensionless mass flow rate	[-]
C_f	Skin friction coefficient	[-]
c_p	Heat capacity at constant pressure	[J/(kg K)]
$D_{i,m}$	Average diffusivity coefficient	[m^2/s]
e	Thermal energy	[J/kg]
E_a	Arrhenius law activation energy	[J/mol]
h	Enthalpy	[J/kg]
h_f^0	Formation enthalpy	[J/kg]
J_i	Diffusive flux	[kg/(m$^2 s$)]
k	Thermal conductivity	[W/(m K)]
L	Characteristic length	[m]
$\dot{m}$	Mass flow rate	[kg/(m$^2 s$)]
m_s	Arrhenius law reaction order	[-]
N_s	Number of species	[-]
P	Pressure	[Pa]

q	Heat flux	[W/m^2]
R	Universal gas constant	[J/(mol K)]
r_c	Recovery factor	[-]
$\dot{S}$	Recession velocity	[m/s]
T	Temperature	[K]
v	Velocity	[m/s]
W	Molecular weight	[kg/mol]
X_i	Mole fraction	[-]
y_i	Mass fraction	[-]

Greek letters

ϵ	Volume fraction	[-]
η	Tortuosity	[-]
ι	Blowing correction coefficient	[-]
κ	Permeability	[m^2]
μ	Viscosity	[Pa s]
ν_i	Stoichiometric coefficient	[-]
Π	Pyrolysis gas production rate	[kg/(m$^3 s$)]
ρ	Density	[kg/m^3]
σ	Stefan-Boltzmann's constant	[W/(m$^2 K^4$)]
τ	Viscous stress tensor	[Pa]
ξ	Emissivity	[-]
χ	Marker function	[-]
ψ	Mass fraction of virgin material	[-]
ω	Gas production rate	[kg/(m$^3 s$)]
ω^{het}	Heterogeneous reaction rate	[kg/(m$^3 s$)]

Subscripts

a	Ablative material
c	Char
e	Boundary layer edge properties
f	Carbon fibers
g	Gas phase
m	Polymer (resin) matrix

s Solid phase

w Wall properties

Non dimensional numbers

C_h Stanton number for heat transfer

C_m Stanton number for mass transfer

Le Lewis number

Ma Mach number

Pe Peclet number

Pr Prandtl number

Conventions

$\boldsymbol{u}$ Vector

$\underline{\underline{\boldsymbol{T}}}$ Second order tensor

Abstract

The atmospheric entry of a space vehicle is crucial in a space mission. To survive the extreme entry conditions, the astronauts and the payload are usually protected by an ablative protection system. Atmospheric entry conditions are difficult to reproduce, so numerical methods are used. In this work, a multi-dimensional material response code is developed based on Argo, which is a discontinuous Galerkin tool. The solver can model the in-depth thermal response of an ablative material submitted to a high enthalpy flow. The recession of the material is accounted for using the immersed level-set method from Argo. A method capable of modeling both the material and the flow was already implemented in Argo. This strong coupling approach is accurate, but computationally expensive. Therefore, in the present work, the approach is simplified to develop a material solver only. Mass and energy balance is implemented to model the heat and mass transfer at the surface of the material. Concerning the ablation rate, it is obtained thanks to thermochemical tables. The material response code is verified thanks to several test cases with different levels of complexity. The obtained results, compared with state-of-the-art codes, demonstrate the ability of the solver to treat multi-dimensional ablation problems.

1 Introduction

1.1 Context

On February 1, 2003, the Space Shuttle Columbia blew up in the Texan sky, killing all seven crew members. The cause of this disaster: a tiny piece of foam broke off during launch and damaged the thermal protection system of the left wing [1]. During reentry, a breach in the shield allowed hot gases to enter, and it melted the structure. The wing collapsed, the shuttle lost control and disintegrated with the aerodynamic forces. At a velocity of about $7[km/s]$, the crew could not survive. This example shows how crucial is atmospheric entry during a space mission. Due to the extreme conditions, a small mistake can lead to dramatic consequences.

The scientific community is eager to explore our solar system and learn more about our universe. They are motivated by previous successful missions, such as the Apollo program that placed the first steps on the Moon, or more recently, the Mars 2020 program, with its Perseverance rover to study the Martian surface. For the future, there are many ambitions. For example, in partnership with other space agencies, NASA is currently working on the Artemis program. The aim is to return and establish a sustainable human presence on the Moon. They also want to create the Lunar Gateway: a space station in lunar orbit. The long-term goal is to make crewed missions to Mars and beyond feasible.

For a space mission to be successful, there are many steps to undergo, but the most challenging phase is probably the entry of the vehicle into the atmosphere at hypersonic velocity [1]. During entry, the spacecraft is submitted to a high heat environment due to the dissipation of the enormous amount of kinetic energy into thermal energy. For the crew to survive and preserve the payload, the vehicle is protected by a thermal protection system (TPS). There are two main types of TPS used nowadays: reusable and ablative materials [2].

- **Reusable materials** are generally best suited for low heat flux trajectories [2]. This type of protection system consists in an insulating material that absorbs and radiates the heat away from the vehicle. A good example is the Space Shuttle's heat shield, which was made of radiation reflective ceramic tiles. Recently, new reusable TPS technologies have been investigated. SpaceX is currently working on Starship, a fully reusable spacecraft designed for future orbital and interplanetary flight. The Starship protection shield is expected to withstand multiple atmospheric entries. Fig. 1.1 shows the Starship SN20 at SpaceX Boca Chica Launch Site. One can observe the reusable thermal protection system made of ceramic tiles placed over the body and the flaps. The black color of the tiles allows to increase the surface emissivity for better radiative cooling.

Fig. 1.1: Picture of Starship heat shield taken by M. McConnaughey at Boca Chica.

[1] For Earth atmospheric entry, the velocity can reach between 7 and $12[km/s]$, depending on the orbit from where the spacecraft comes from. The entry velocity can be even more extreme, for example, $47.4[km/s]$ for the Galileo space probe that entered Jupiter's atmosphere in 1995

- **Ablative materials** are often more advantageous for higher entry velocities [2]. They are made of composite materials; generally carbon fibers impregnated with resin. During entry, they degrade to protect the vehicle, and they decompose into gases that carry away some of the heat by convection. Orion (the crewed spacecraft of the Artemis program) is equipped with this type of material [3]. It is a suitable choice since the spacecraft will have to withstand an Earth entry velocity of about $11[km/s]$ (when it will come back from Lunar orbit). Orion uses a high-density ablative material called AVCOAT (see Fig. 1.2a).

  For a better mass efficiency, low-density ablative materials are developed, such as PICA (Phenolic Impregnated Carbon Ablators) which is a promising ablator tested during the NASA Stardust Mission [4]. For example, the Dragon capsule that brings back astronauts from the ISS uses PICA-X (a SpaceX variant of PICA). Fig. 1.2b shows the Dragon spacecraft and its PICA-X heat shield after splashdown. The TPS degraded during entry, and one can see that the surface is carbonized.

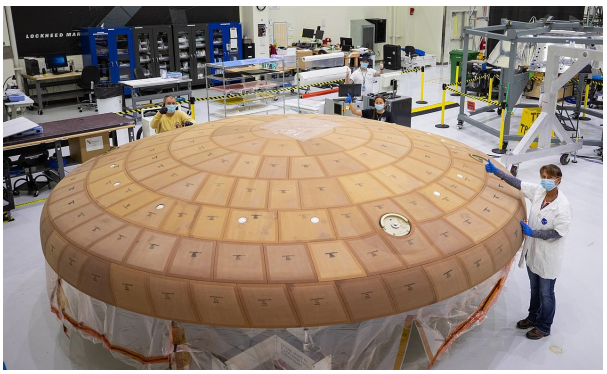

(a) Technicians inspecting the AVCOAT heat shield of the Orion spacecraft. Picture taken from the NASA's Kennedy Space Center Report from 2020.

(b) SpaceX Dragon spacecraft and its degraded PICA-X TPS after splashdown. Picture taken by C. Hudson.

Fig. 1.2: Examples of ablative TPS on the Orion and SpaceX Dragon spacecraft.

Designing a space vehicle, particularly its thermal protection system, is a real challenge. The prediction of the heat exchange at the TPS surface during entry is complex because many phenomena have to be taken into account: radiation, gas-surface interactions, shape change due to recession, pyrolysis, etc. There are two main quantities to estimate for the design of a TPS for a given mission: the peak temperature at the interface with the underneath structure and the total surface recession. It is difficult to evaluate precisely those quantities, and thus a common practice is to use an excessive safety factor for the thickness of the TPS. This technique is not efficient because it increases the mass of the spacecraft.

Moreover, it is complicated and expensive to reproduce entry flight conditions on Earth. The use of numerical methods is thus the key to understand the physics of atmospheric entry and to develop design tools for thermal protection systems.

1.2 Physics of the atmospheric entry

The space vehicle enters the atmosphere with an extreme velocity and progressively decelerates by dissipating the kinetic energy into thermal energy. Depending on different parameters such as the entry velocity, the aerodynamic regime, or the spacecraft's shape, a certain fraction of the heat is transferred to the vehicle [2].

Before entering into details about the physics of the atmospheric entry, Table 1.1 shows orders of magnitude for the thermal energy transferred to some famous space vehicles during entry. Those energy density are huge knowing for example that the latent heat of vaporisation of water (at $1[atm]$ and $100[°C]$) is $2.25[MJ/kg]$ [5].

Table 1.1: Entry velocity and energy density transferred during entry (data from [2]).

Vehicle	Entry velocity $[km/s]$	Energy density $[MJ/kg]$
Apollo	11.4	66
Mars Return	14	98
Galileo	47.4	1130

1.2.1 Reactive shock layer

The different processes occurring during atmospheric entry are illustrated in Fig. 1.3 and explained in detail by Schrooyen [6]. the spacecraft enters the atmosphere[2] at hypersonic velocity, which means that the local flow velocity is five times higher than the speed of sound in the medium ($Ma > 5$). When the altitude decreases, the atmosphere becomes denser, and the vehicle progressively decelerates to finally reach a subsonic regime ($Ma < 1$). When the Mach number is higher than one, a curved **reactive shock layer** is formed in front of the vehicle. The thickness of the shock layer is about tens of centimeters, and it decreases with higher velocities. This shock layer includes a thermal and viscous boundary layer, formed close to the heat shield, with a thickness of micrometers to millimeters [6]. A sketch of the shock and boundary layer around the Orion spacecraft is shown in Fig. 1.3.

Outside the shock layer, the gas particles behave as a freestream flow at low temperature, high velocity, and low density. For example, for the Earth atmospheric entry of the Orion spacecraft, the characteristics of the freestream flow are given in Fig. 1.3. Through the shock, the kinetic energy is transformed into vibrational, translational, rotational, and electronic energy [6]. Inside the shock layer, the flow is dense, and the temperature is extreme (the temperature can reach up to $10\ 000[K]$). The shock layer contains thus a high enthalpy flow which provokes fast chemical reactions, including:

- Molecular dissociations (e.g.: $O_2 \rightarrow 2O$).
- Combination reactions (e.g.: $O_2 + N_2 \rightarrow 2NO$)
- Atomic and molecular ionizations. (e.g.: $NO \rightarrow NO^+ + e^-$).
- Vibrational excitation and de-excitation of the electrons leading to radiation.

[2] For example, the boundary between Earth's atmosphere and outer space is located at the Kármán line, at an altitude of $100[km]$.

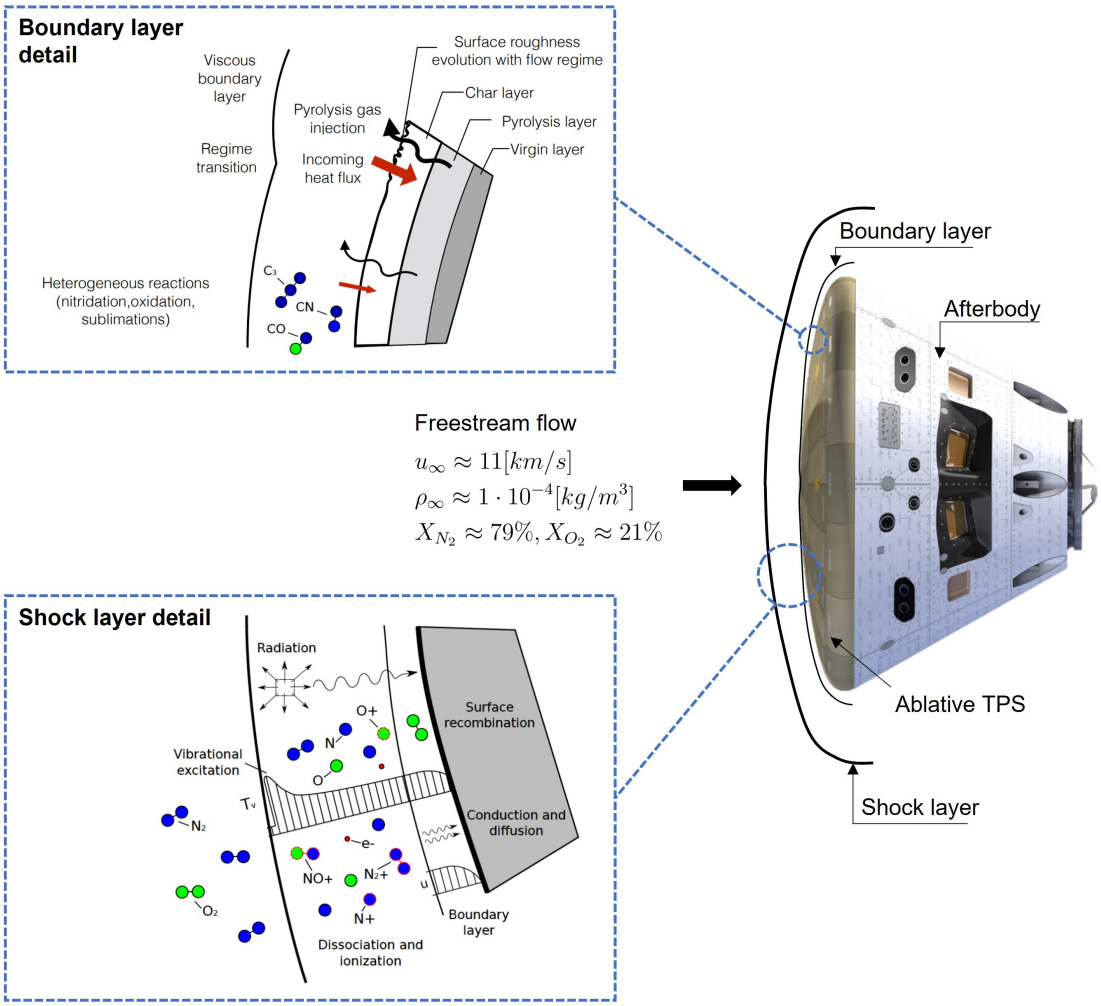

Fig. 1.3: Sketch of the processes occurring during atmospheric entry in the shock layer and at the surface of a space vehicle (such as the Orion spacecraft represented here). Figure modified from Schrooyen [6] and Potter [7], illustration of Orion from [3].

1.2.2 Degradation phenomena of the ablative material

The radiation (due to the excitation/de-excitation of the electronic population in the shock layer) and the convection of the high enthalpy flow heat up the ablative material. The heat is transferred in-depth by conduction, and the temperature increases gradually. The temperature at the surface can reach up to 3000$[K]$ for high entry velocities [6]. Due to the temperature rise, the material degrades by two phenomena that allow to absorb the heat: the pyrolysis of the resin and the ablation/erosion of the remaining char and the carbon fibers.

The PICA ablative material will be used for the following explanations as an example. As a reminder, PICA is a composite material made of carbon fibers impregnated with a phenolic resin. It is a low-density ablative material that is highly porous.

[3] `https://bit.ly/30gOxJJ`

1. The **pyrolysis** is the first degradation phenomenon. It is a thermal decomposition reaction that starts when the temperature of the virgin material reaches about $200[°C]$ for PICA [8]. During the pyrolysis process, the resin progressively carbonizes and produces pyrolysis gases. Those gases are transported out of the porous material by diffusion/convection and blown into the boundary layer. The pyrolysis will degrade the material, but it will help to reduce the heat load and protect the structure thanks to different phenomena.

   The first advantage is that the reaction is endothermic, so it will absorb a part of the heat. Moreover, the blowing of the pyrolysis gases into the boundary layer will induce a blocking effect of the convective heat flux and further reduce the heat load. Finally, the gases carry carbon species such as CO or C_3, which makes the boundary layer more opaque and therefore reduces the radiative heat flux [6, 9]. At the end of the pyrolysis reaction, it remains a char zone composed of the carbonized resin and the carbon fibers.

2. The second degradation phenomenon is the **ablation/erosion of the char**. During this degradation phase, the fibers and the charred resin are degraded by the high enthalpy flow due to mechanical and thermochemical reactions. The ablation may be due to different processes depending on the entry conditions (entry velocity, flow regime, etc.), the planet atmosphere composition, and the properties of the TPS material:

   - **Heterogeneous chemical reactions:** The carbon from the char zone reacts with the oxygen (oxidation) or with the nitrogen (nitridation) present in the boundary layer. The heterogeneous reactions depends on the planet atmosphere composition. For example, for an Earth atmospheric entry:

$$\left.\begin{array}{l} C_{(s)} + O_{2(g)} \longrightarrow CO_{2(g)} \\ C_{(s)} + O_{(g)} \longrightarrow CO_{(g)} \end{array}\right\} \text{ Oxidation}$$
$$\left.\begin{array}{l} C_{(s)} + N_{(g)} \longrightarrow CN_{(g)} \end{array}\right\} \text{ Nitridation}$$

   - **Phase change (sublimation):** In the case of extreme entry conditions, the temperature can become sufficiently high for the carbon to sublimate (the sublimation of carbon species will produces gases such as C_2 or C_3).

   - **Mechanical ablation (spallation):** The mechanical shear stress due to the friction forces at the wall or the impacts can eject fragments of material and participate to the recession. To reduce this spallation phenomena, the TPS materials are often reinforced to withstand high thermo-mechanical stresses [10].

Fig. 1.4 shows a picture of a core of PICA recovered from the Stardust spacecraft. The degradation zones are illustrated, and Scanning Electron Microscope images show the material response at different depths. On the SEM images, the different degradation zones can be observed. Close to the substructure, the material is virgin; one can see the carbon fibers impregnated with the phenolic resin. In the middle of the pyrolysis zone, some resin is charred due to the pyrolysis. In the char zone, the PICA is completely carbonized; the charred resin and the carbon fibers can be distinguished. Finally, on the TPS surface, the carbonized material is partially ablated (the charred resin has been removed due to ablation, and the carbon fibers are eroded).

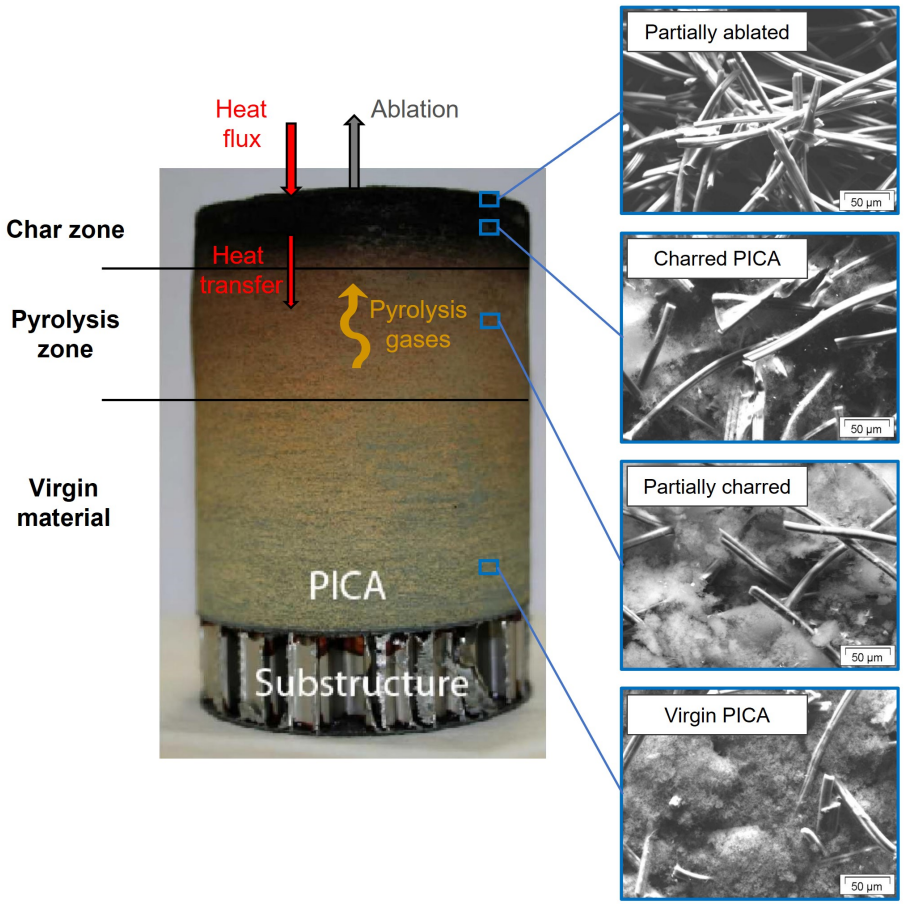

Fig. 1.4: Picture of a core of TPS recovered from Stardust (picture from [4]). Sketch of the different degradation zones and Scanning Electron Microscope images (from [11]) showing the material response of PICA at different depth.

1.2.3 Gas-surface interactions

The material response problem is challenging since many dynamic interactions exist between the material and the flow. The gas-surface interactions are described in detail by Schrooyen in [6]. As explained in Section 1.2.2, the flow in the boundary layer erodes the TPS surface due to heterogeneous reactions, phase changes, or mechanical ablation (spallation). The pyrolysis gas also interacts with the chemical species present in the boundary layer through homogeneous reactions. Moreover, catalytic reactions and recombinations of the dissociated species (e.g. $O + O \rightarrow O_2$) can occur at the interface between the material and the flow.

On the other hand, the surface roughness changes due to erosion, which induces different phenomena. The roughness influences the flow regime, and it may produce a transition towards turbulent flow. If the flow becomes turbulent, the heat and mass exchange will increase and hence induce more recession. Furthermore, the shape of the ablative material changes with the recession, which may modify the vehicle's aerodynamic properties [6].

The problem is even more complex for low-density ablative materials such as PICA. Due to the high porosity, the flow from the boundary layer can percolate through the pores of the material and erode the fibers in-depth. In addition to the **surface ablation** there is thus also what is called **volume ablation** [6]. The in-depth erosion will weaken

the fibers leading to less mechanical strength. It will increase spallation at the surface and therefore contribute to the recession. The difference between surface and volume ablation can be observed in Fig. 1.5. This numerical simulation shows the erosion of carbon preform for two different regimes [12]. For the diffusion regime in Fig. 1.5a, the surface ablation prevails over volume ablation (at the end, the fibers on the surface are totally ablated, and the fibers remain relatively intact in-depth). For the reaction regime in Fig. 1.5b, volume ablation is dominant (the fibers are eroded in-depth, they are not mainly ablated on the surface).

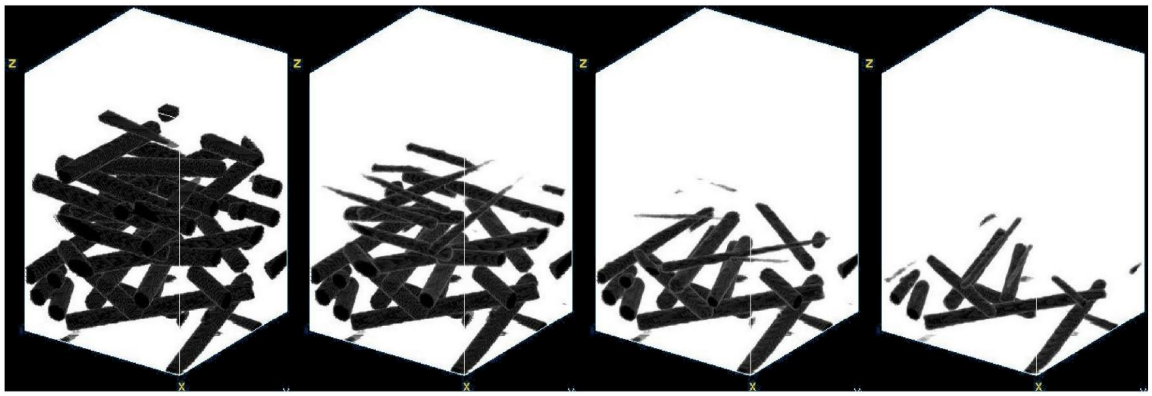

(a) Diffusion regime: $p = 10[atm]$, $D/k = 50[\mu m]$

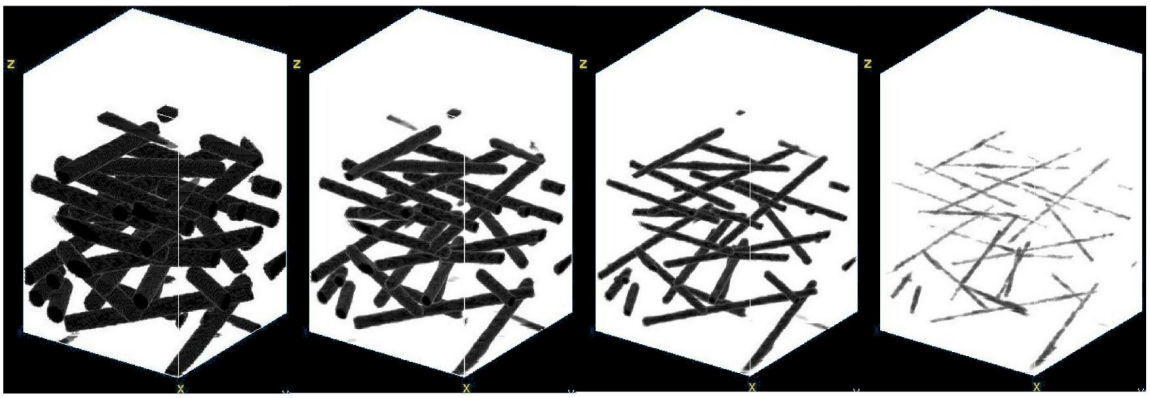

(b) Reaction regime: $p = 0.26[atm]$, $D/k = 2[mm]$

Fig. 1.5: Numerical simulation of the erosion of carbon preform submitted to two different regimes. Figure from [12].

Predicting accurately the transient response of an ablative material is thus highly complex due to the strong dynamic interactions between the material and the flow. There are two main approaches to solve this problem: strong coupling or the use of transfer coefficients. Strong coupling solves both the material and the flow with a unified method. This technique provides accurate results, but it is computationally expensive. On the other hand, the transfer-coefficients approach (used in this work) simplifies the problem by using heat and mass transfer coefficients. Those coefficients allow to model the convective flux and the mass transfer at the surface. In this case, thermochemical tables are used to provide the ablation rate. This method reduces the computational costs and provides a good approximation, but some phenomena such as volume ablation are not considered. More details about the different numerical approaches are given in the further sections.

1.3 State-of-the-art

As explained in Section 1.2, designing a space vehicle and especially its thermal protection system is a crucial and challenging task. It is essential to deeply understand the different phenomena occurring during atmospheric entry and accurately predict the ablative material's response to guarantee a safe space mission. To reach this goal, experimental methods and numerical simulations are used in parallel. This section will present an overview of the different experiments and numerical approaches. Finally, the state-of-the-art of existing material response codes will be detailed.

1.3.1 Experimental methods

Reproducing experimentally atmospheric entry conditions is extremely complex. Nevertheless, there are two approaches to conduct experiments. The first one consists in equipping the space vehicle and its thermal protection system with various instruments and collecting data. This method is efficient, but it is costly, mainly due to the costs of a rocket launch. The other approach is to try to reproduce the atmospheric entry conditions on Earth thanks to different facilities such as a hypersonic wind tunnel or a plasmatron. The idea of this method is to mimic some realistic flight conditions.

In-flight experiments are rare, but they provide interesting data to develop the TPS technologies further. Some European and Worldwide experiments can be highlighted:

- The FIRE II capsule launched in 1965 and developed by NASA was dedicated to study the atmospheric entry's impact on the spacecraft materials. It was able to measure the radiative heat flux thanks to calorimeters and radiometers.
- The Atmospheric Reentry Demonstrator (ARD) is a suborbital entry vehicle developed by the European Space Agency. It performed a spaceflight in 1998, and the goal of the mission was to investigate different entry technologies and better understand some phenomena occurring during atmospheric entry.
- The Intermediate eXperimental Vehicle (IXV) is an ESA entry vehicle launched in 2015 (see Fig. 1.6). The objective was to show the improvements in the field of reusable orbital return vehicles. The thermal protection system was equipped with various instruments such as thermocouples and displacement sensors [13].
- Galileo, Mars PathFinder, and MSL space probes were equipped with different instruments to analyze the response of their thermal protection system. The data collected allowed to learn more about the response of ablative materials.

Moreover, interesting data can also be obtained by analyzing samples of degraded thermal protection systems after an atmospheric entry. A famous example is the Stardust mission. A PICA TPS protected the Stardust capsule, and it performed a reentry in 2006 after an interplanetary flight of 4.5 billion kilometers (see Fig. 1.7) [14]. During its journey, it collects comet and interstellar dust particles. It enters Earth's atmosphere at an extreme velocity of $12.8[km/s]$, which is up to now the fastest Earth's atmosphere entry velocity for a space vehicle. A core of TPS recovered from the Stardust capsule is shown in Fig. 1.4. The total recession can be measured, and the different degradation zones can be observed with a microscope. Analyzing degraded samples of ablative materials allows to better understand phenomena such as pyrolysis or ablation (fibers erosion).

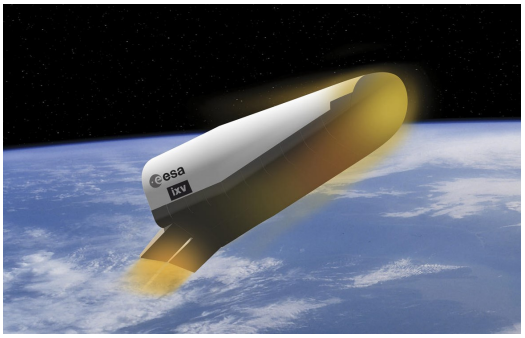

Fig. 1.6: Artistic view of the Intermediate eXperimental Vehicle during atmospheric entry. Figure from ESA made by J. Huart.

Fig. 1.7: Sample return capsule from NASA's Stardust mission. Picture from NASA[4]taken after landing in Utah [14].

Experiments can be conducted on Earth thanks to several facilities available across the globe. It is impossible to mimic all the extreme conditions of an atmospheric entry, but some realistic flight conditions can be reproduced. The principal facilities with their respective abilities are:

- **Hypersonic wind tunnels** are used to study the aerodynamics of space vehicles during atmospheric entry but also hypersonic aircrafts, missiles, etc [15]. For instance, it allows to study the compression shocks or the boundary layer effects. Those facilities can generate hypersonic flow typically from Mach 5 to 10. For the experiment, the energy is generally stored in compressed gas and then released for a short time. Therefore, the running time of the test is often limited to a few seconds.
- **Arc jets and plasmatrons** are intended to reproduce the high enthalpy environment encountered during atmospheric entry. It is used, for instance, to analyze the response of thermal protection systems. The sample is submitted to a high enthalpy flow (such as plasma), and data are collected thanks to different instruments like thermocouples. In the case of a plasmatron, the plasma is generated with a high-frequency inductive coil [6]. An example of a plasmatron facility during an ablation test is shown in Fig. 1.8. It is the plasmatron from the von Karman Institute. A sample of ablative material submitted to the plasma jet can be observed.

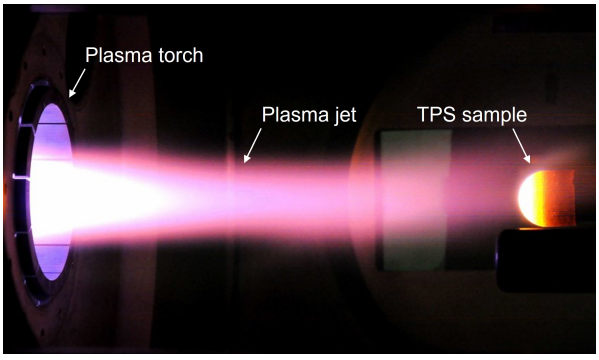

(a) Plasmatron chamber during an ablation test. The plasma jet and the TPS sample can be observed.

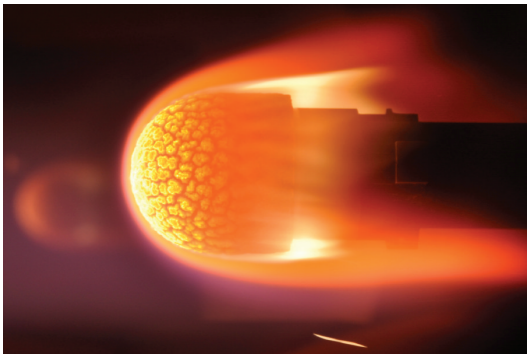

(b) Zoom on the sample of ablative TPS submitted to the plasma jet.

Fig. 1.8: Pictures of the plasmatron facility from the von Karman Institute during an ablation test. Pictures taken by B. Helber.

[4] `https://go.nasa.gov/39YpxHu`

1.3.2 Numerical approaches

There are various numerical approaches to model the response of an ablative material during atmospheric entry. Each method has its advantages and drawbacks. An overview of the different techniques will be given in this section. Four types of solvers can be distinguished:

1. **Material solver:** The material solver approach is the one used in this work. In this strategy, the transient thermal response of the material is computed thanks to a solver that focuses on the solid side of the problem. Simplified boundary conditions are used at the interface between the material and the flow. Typically, as explained in Section 2.3, energy and mass balance are implemented to compute the heat and mass transfer at the surface. Moreover, transfer coefficients are used to model, for instance, the convective heat flux from the boundary layer. The transfer coefficients are computed beforehand thanks to simplified flowfield simulations. The surface conditions (e.g. the convective heat flux) are found thanks to semi-empirical relations. In the literature, many material codes have been developed with different capabilities and levels of fidelity. A review of existing material response code is given by Lachaud et al. in [8] and summarized in Section 1.3.3.

2. **Flow solver:** This solver focuses on the flow and models the ablation of the material with simplified methods. The flow is computed by solving Navier-Stokes equations thanks to a CFD software. Concerning the material, surface ablation is modeled using a particular boundary condition at the gas-solid interface. Once the flow characteristics are known, the heat transfer in the material can be computed considering surface mass and energy balance. Several flow solvers have been developed and demonstrated for various applications [16, 17, 18, 19].

3. **Weakly coupled solver:** In this type of solver, there is a tool to compute the characteristics of the flow and another to solve the thermal response of the material. Both tools are separate, and information is shared at the boundary between the material and the flow. The coupling is "weak" since data exchange at the boundary is done at defined time steps during the simulation. Different weakly coupled solvers exist in the literature with different techniques for the exchange at the boundary [20, 21, 22, 23].

4. **Strongly coupled solver:** In the strong coupling approach, both the material and the flow are computed within a unified tool. The gas and solid phase problems are solved in the same computational domain. In opposition to the weak coupling method, the interactions between the material and the flow are captured in a time-accurate way (not at particular time steps like for the weak coupling). Due to the complexity of the implementation, only a few solvers are based on the strong coupling approach [6, 24, 25, 26].

The two first approaches focus on a particular problem, either the material or the flow. The first method provides accurate results for the material response, but some gas-surface interactions are not considered, such as volume ablation. The boundary layer is modeled in a simplified manner thus some phenomena are not considered. On the other hand, for flow solvers, the phenomena occurring in the fluid region are well captured, but the prediction of the degradation of the material is inaccurate. Many material and flow solvers exist in the literature, and their abilities have been demonstrated in different cases.

Nevertheless, when the ablation rate is high (particularly for extreme entry conditions), there are many gas-surface interactions, and a coupled approach is preferred to obtain accurate results [6].

The weak and strong coupling approaches allow to better model the interactions between the material and the flow. However, for weakly coupled solvers, the exchange of information is done at specific time steps; thus, instabilities may appear. In fact, the ablation problem is complex and highly non-linear. The strong coupling is certainly the best approach to model accurately the gas-surface interactions, but it is complex and computationally expensive.

1.3.3 Material response codes

Overview

Several simulation tools exist to model the response of ablative materials during atmospheric entry. Some are developed for research and development, and others are used for design purposes. An overview of the different material response codes is presented in this section, and the interested reader can refer to the paper of Lachaud et al.[8] for more detail.

Most material response codes inherit from models developed in the 1960s. In particular, they rely on the Aerotherm report from 1968 and especially the CMA model [27]. This model is among the first in-depth material response codes. It includes many assumptions, and some phenomena are neglected. Encouraged by challenging space missions, the scientific community is trying to improve these models to reach a higher level of fidelity. To achieve this goal, experiments have been conducted (see Section 1.3.1), and the pyrolysis and ablation problems have been investigated.

There are two approaches to increase fidelity. The first method is to develop new models to consider physical phenomena neglected in the 1960s. For instance, some codes are improved to take into account finite rate chemistry [28], mechanical ablation [29], radiation [30], etc. For porous materials, new diffusion models are developed to model the diffusion of the gaseous species inside the pores [6]. The second approach to increase fidelity is to characterize the material better. Complex models are developed to define the material properties: conductivity, permeability, tortuosity, etc. Many thermal protection materials are orthotropic, which means that the material properties are different in the three perpendicular directions. For example, for PICA, the thermal conductivity in the "thickness" direction is different from the one in the perpendicular plane. To take this into account, some codes develop orthotropic models for the thermal conductivity [31, 32].

The different material response codes can be classified depending on the dimensionality, the level of fidelity, and the maturity [8]. Note that each criterion is gauged from one to three. The dimensionality corresponds to the space dimension of the mesh (1: 1-dimension, 2: 2-dimensions planar or axisymmetrical, 3: 3-dimensions). Maturity relates to the degree of implementation and verification of a particular response code. A maturity of one corresponds to a code verified with limited cases, and a maturity of three concerns mostly design codes. Concerning the level of fidelity, it depends on the complexity of the model implemented. According to [33], three categories can be defined, as follows:

1. **Type I:** They implement the CMA model [27] or an equivalent model from the 1960s. They model the heat transfer in the material and the decomposition due to pyrolysis. A simplified approach is used to model the transport of the pyrolysis gas, and many phenomena such as volume ablation are not considered. In type I codes, three main hypotheses are used: thermal equilibrium is assumed between the solid, and the gaseous phase, the direction of the pyrolysis gas is perpendicular and direct toward the surface, and the residence time of the gas inside the control volume is short [6].
2. **Type II:** A more accurate model is used for the transport of the pyrolysis gas through the pores. The average momentum equation (Darcy's law) is implemented, and it allows to determine the direction of the flow (the second hypothesis of type I codes is removed).
3. **Type III:** It includes higher fidelity codes which add improvements with respect to type II. They can treat, for instance, multi-component diffusion, radiative heating, finite-rate chemistry, etc.

Fig. 1.9 shows illustrations of the macroscopic and microscopic phenomena occurring during the degradation of a charring ablative material submitted to a high enthalpy flow [28]. It also indicates which phenomena are taken into account by material response codes depending on their level of fidelity.

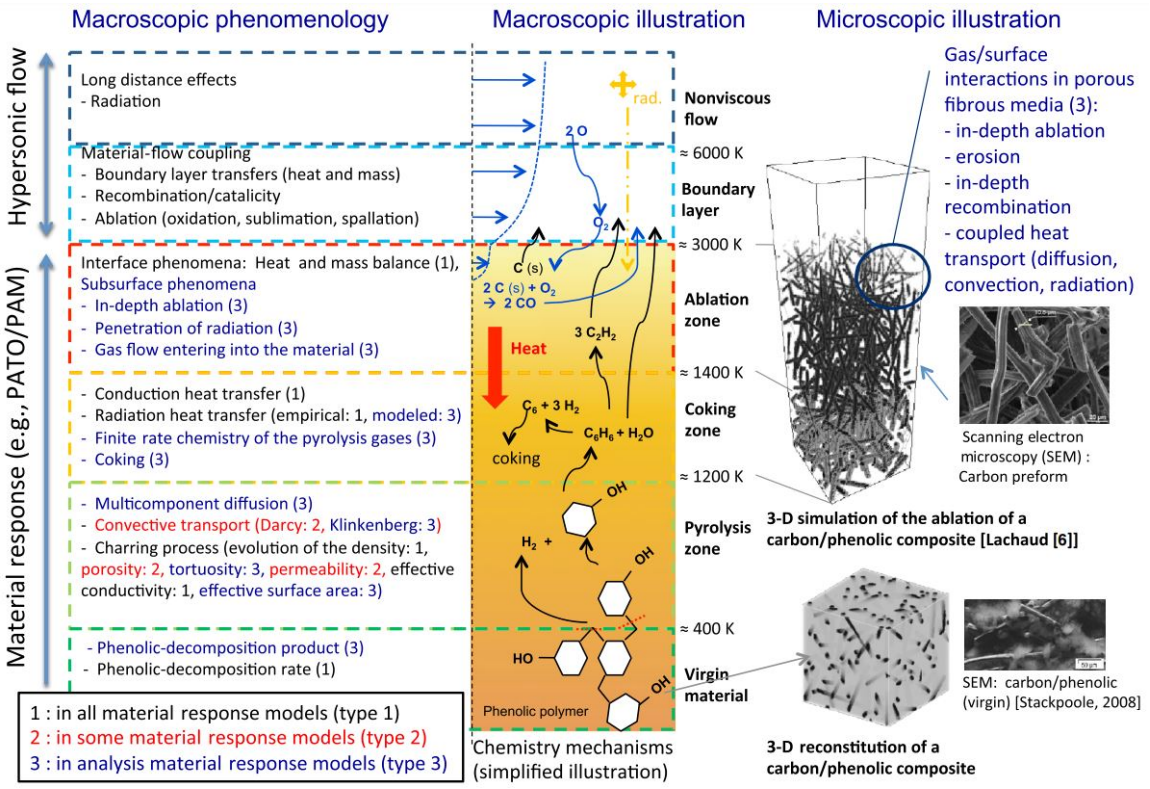

Fig. 1.9: Macroscopic and microscopic phenomena occuring during the degradation of an ablative material submitted to a high enthalpy flow. Figure taken from [28].

Description of some existing codes

During the past two decades, the NASA Ames Research Center developed a set of tools to model the response of TPS materials. It includes FIAT [34], TITAN [35] and 3dFIAT [36] which are respectively in one, two and three dimensions. NASA and SpaceX employ FIAT as a one-dimensional tool for the TPS design of space vehicles. TITAN is used to analyze two-dimensional planar or axisymmetrical problems. 3dFIAT is used for in-depth analysis and when two-dimensional analyses are not adequate. It allows to reach a high-level fidelity, but it is computationally expensive. For instance, with 3dFIAT, the thermal response of a TPS can be computed for a particular angle of attack of the spacecraft during atmospheric entry [37]. Several versions of those codes have been developed to increase the fidelity. For example, FIAT has been improved to predict shape change due to recession [38] or to consider chemistry nonequilibrium of pyrolysis gas [39]. Concerning TITAN and 3dFIAT, they have both be improved to consider for instance orthotropic thermal conductivity [31, 32].

Another tool that can be highlighted is PATO [28] which is a library based on OpenFOAM (an open-source CFD software). PATO allows to model the response of any porous material (especially ablative materials) submitted to high enthalpy environments. It implements a high-fidelity model that considers multi-component diffusion, in-depth ablation/coking, viscous dissipation, finite-rate chemistry, etc. It is flexible, and it can be used to implement or test new models[5]. PATO contains two main modules. One module is dedicated to global analysis, and another is used for elementary analysis. The global analysis module is used to model the full response of an ablative material considering a macroscopic point of view. On the other hand, the elementary analysis module allows to study microscopic phenomena such as the erosion of the carbon fibers.

Most material response codes consider heat and mass exchange as surface phenomena only. In particular, volume ablation is usually neglected. This strong assumption leads to inaccurate results, especially for highly porous materials (such as PICA). A few works propose solutions to account for in-depth ablation. In particular, to model this complex phenomenon, Schrooyen developed a new ablation module in Argo [6]. Argo is a multi-physics platform developed by Cenaero. It is based on a Discontinuous Galerkin Method (DGM[6]), and it can treat convection, diffusion, and reaction problems. The DGAblation module allows to model the response of an ablative material submitted to a high enthalpy flow. It uses on a strong coupling approach; hence it accurately captures the solid-gas interactions. The code can account for finite rate chemistry, heterogeneous reactions, volume ablation, etc. This high-fidelity model provides accurate results, but it is computationally expensive.

At Cenaero, Echion, a one-dimensional tool, has also been developed. Its structure is similar to Argo, and it can deal with convection, diffusion, and reaction problems. It was created initially by Gorissen [40] and improved by Schrooyen et al. [41] to model the in-depth thermal response of ablative materials. It can deal with recession thanks to a moving mesh algorithm. Echion is a pure material solver validated with different one-dimensional ablation test cases. The main objective of Echion was to investigate the abilities of the material solver approach.

[5] In this work, PATO will be used as a reference for the test cases

[6] DGM combines the advantage of finite element and finite volume method. It provides good computational efficiency and accuracy on unstructured meshes.

1.4 Objectives

In his PhD thesis, Schrooyen [6] developed a strong coupling approach to solve both the material and the flow. This high-fidelity method is accurate, but it is computationally expensive. The objective of the present work is to simplify the approach and develop a material solver only. The idea is to implement new boundary conditions in Argo to model the heat and mass exchanges at the surface between the material and the flow. Surface mass and energy balance will be implemented, and transfer coefficients will be used to model the convective flux and the mass transfer at the gas-solid interface. Thermochemical tables will allow to compute the ablation rate, and the recession of the material will be accounted for using the immersed level-set method implemented in Argo. The objective is to investigate and demonstrate the abilities of a material solver approach for 1-dimension and 2-dimensions axisymmetrical ablation problems. Note that the solver will inherit from the efficiency of Argo and its discontinuous Galerkin method to solve systems of partial differential equations.

This work is divided into five chapters. After the introduction, chapter 2 describes the physical modeling. The equations used to solve the response of an ablative material are presented. The constitutive equations (mass, momentum, and energy conservation) are detailed then the focus is placed on the boundary conditions. The surface mass and energy balance implemented in this work are described, and the transfer coefficient approach is explained. This chapter also presents the methodology used to obtain the ablation rate thanks to thermochemical tables. The third chapter explains the numerical method used to model recession. It presents an overview of existing immersed methods, and the level-set method from Argo is described. Chapter 4 is dedicated to the presentation of the results. The abilities of the material solver are demonstrated and tested thanks to various test cases. Results for 1-dimension and 2-dimensions axisymmetrical cases are presented and described. Different aspects are tested: the thermal transfer, the blowing of pyrolysis gas and ablation products, the recession, etc. To conclude, the last chapter highlights the achievements of the master thesis and provides an overview of the perspectives.

2 Physical modeling

2.1 Introduction

In this work, an ablative material made of carbon fibers impregnated with resin is considered (see Section 1.1). The material is highly porous, and it has a low mass density. During atmospheric entry, due to the high heat load, the temperature will gradually increase, and the material will degrade. The resin will pyrolyze, producing gases that will percolate through the pores of the material. The remaining char and the carbon fibers will degrade by erosion, and the surface will recede. Modeling the response of such an ablative material is complex since it depends on many phenomena: thermal conduction, degradation, chemical reactions, etc. Nevertheless, for the design of a TPS, it is essential to predict accurately (i) the temperature at the interface with the substructure and (ii) the total recession.

As explained in detail in Section 1.3.3, many ablative material response codes exist with different levels of fidelity and dimensionality. In Argo, a type III ablation model is implemented, and it can handle multi-dimensional cases (1-dimension, 2-dimensions planar or axisymmetrical, or 3-dimensions). This chapter will explain the constitutive equations and the boundary conditions used to model the in-depth thermal response of an ablative material. The constitutive equations (mass, momentum, and energy conservation) were already implemented in Argo. Therefore, the focus will mainly be placed on the boundary conditions, particularly the surface mass and energy balance, implemented and added during this work. The last part of this chapter will explain the methodology to compute the ablation rate using thermochemical tables.

Before going further, the author would like to thank J. Lachaud et al. [8], P. Schrooyen [6], and D. Bianchi [10] for their detailed explanations about the physical modeling of ablative materials submitted to a high enthalpy flow.

2.2 Constitutive equations

2.2.1 Mass conservation equation

Gaseous phase mass conservation

During pyrolysis, the resin will decompose into gases that will be injected into the boundary layer. Indeed, since the material is highly porous, the gases will pass through the pores of the material. Moreover, gaseous species can also appear due to homogeneous reactions (between the gaseous species in the pyrolysis gas or with the species in the boundary layer) or heterogeneous reactions. The objective is to track those gaseous species to satisfy the gaseous phase mass conservation equation. For models with a high level of fidelity ([6, 28]), all gaseous species are tracked independently. This approach is the most accurate, but it leads to more equations (one equation per species). As explained by Schrooyen [6], if a general multi-dimensional case is considered, the mass conservation equation for a gaseous species i (in a set of gaseous species S) is given by

$$\underbrace{\frac{\partial\left(\rho_i \epsilon_i\right)}{\partial t}}_{\text{Conservative term}} + \underbrace{\nabla \cdot \left(\rho_i \epsilon_i \boldsymbol{v_g}\right)}_{\text{Convective term}} + \underbrace{\nabla \cdot \boldsymbol{J_i}}_{\text{Diffusive term}} = \underbrace{\Pi_i + \epsilon_i \omega_i}_{\text{Source terms}}, \; \mathrm{i} \in S, \tag{2.1}$$

where ρ_i is the mass density of the species i, ϵ_i is the volume fraction, $\boldsymbol{v_g}$ is the interstitial

flow velocity of the pyrolysis gas, and $\boldsymbol{J_i}$ is the diffusive flux. Concerning the source terms, Π_i is the gas production rate due to the decomposition of the resin by pyrolysis, and ω_i is the gas production rate due to chemical reactions. To solve the mass conservation equation, it is needed to know the pyrolysis gas velocity $\boldsymbol{v_g}$ (and its direction) [8]. In one-dimensional models, the direction of the gas velocity is often assumed to be perpendicular to the surface and directed towards the surface. For multi-dimensional models, $\boldsymbol{v_g}$ is computed thanks to the momentum conservation equation [6].

The diffusive flux $\boldsymbol{J_i}$ is due to the diffusion of the species i in the gaseous mixture within the porous medium. The diffusion term is not negligible compared to the convective term (particularly at low pressure) [8]. $\boldsymbol{J_i}$ is complex to evaluate, but it can be modelled thanks to the Fick law (Eq. (2.2)) [6]. A Ramshaw projection is used to implement the species diffusion term; this ensures that the sum of all the diffusive flux is null, and so the total mass is conserved [42].

$$\mathbf{J}_i = -\epsilon_i \rho_i \frac{D_{i,m}}{\eta} \frac{W_i}{W} \nabla X_i + \epsilon_i \rho_i \sum_{k=1}^{N_s} \frac{D_{k,m}}{\eta} \frac{W_k}{W} \nabla X_k. \tag{2.2}$$

In Eq. (2.2), $D_{i,m}$ stands for the average diffusivity coefficient of the species i in the mixture, η is the tortuosity (length ratio between the real trajectory of a particle between two points in the porous medium and a straight line), and N_s is the number of species in the mixture. W and X are, respectively, the molecular weight and the mole fraction.

To reduce the number of equations and thus simplify the computation, some models (type I and II) do not track every gaseous species, but they consider an overall pyrolysis gas. In this case, Eq. (2.1) becomes

$$\frac{\partial \left(\rho_g \epsilon_g\right)}{\partial t} + \nabla \cdot \left(\rho_g \epsilon_g \boldsymbol{v_g}\right) = \Pi. \tag{2.3}$$

The system of N_s equations is now reduced to a simplified unique equation. Considering an overall pyrolysis gas, the diffusive term and the source term due to chemical reactions vanish. The equation is expressed in terms of an overall mass density ρ_g, a volume fraction ϵ_g, and a pyrolysis gas production rate Π.

Solid phase mass conservation

Due to the temperature rise, the resin is decomposed into pyrolysis gas. Note that the resin is made of different components with different properties. Each component has a specific mass density and different pyrolysis decomposition. The decomposition rate of a resin component is equal to the production rate of pyrolysis gases Π. To compute Π, Arrhenius laws are used to fit thermogravimetry analysis of the resin decomposition [6, 43]

$$\frac{\partial(\rho_m \epsilon_m)}{\partial t} = -\Pi = -A_s \cdot \exp\left(-\frac{E_a}{RT}\right) \rho_0 \left(\frac{\rho_s - \rho_r}{\rho_0}\right)^{m_s}, \tag{2.4}$$

where ρ_m is the mass density of the resin (matrix) component, A_s is a pre-exponential factor, E_a is the activation energy, R is the universal gas constant, and m_s is the reaction order. ρ_0 and ρ_s are the initial and the instantaneous mass density of the resin component. Concerning ρ_r, it is the residual mass density (the mass density of the charred resin component).

In this work, a three-components decomposition model from Goldstein [43] is used. The material is assumed to be composed of carbon fibers and two phenolic resin components (called A and B). Table 2.1 shows the different constants for the pyrolysis decomposition of TACOT (Theoretical Ablative Composite for Open Testing). TACOT is a theoretical material with thermochemical properties similar to current low-density ablators. This material is used for all the test cases presented in this paper [33, 44, 45].

Table 2.1: Decomposition kinetics model for TACOT (data from the spreadsheet of the ablation test cases from Lachaud et al. [33, 44, 45]).

Reaction	ρ_0 $[kg/m^3]$	ρ_r $[kg/m^3]$	A_s $[s^{-1}]$	E_a $[J/mol]$	m_s $[-]$	T_{reac} $[K]$
A	300	0	$1.20e^4$	$7.11e^4$	3	333.3
B	900	600	$4.48e^9$	$1.69e^5$	3	555.6

Table 2.1 provides interesting information about the decomposition of the two resin components. For example, the residual density ρ_r for the reaction A is zero, which means that during pyrolysis, the resin component A is completely transformed into gases. On the other hand, when the component B will decompose, char will remain since $\rho_r = 600[kg/m^3]$. The last column shows the temperature at which the resin components start to decompose. It can be observed that the component B will begin to pyrolyze at a higher temperature. The interested reader can refer to [43] for detailed explanations about the Arrhenius laws and the Goldstein three-components decomposition model.

Moreover, the solid species at the surface (typically the carbon species in the char zone) are also degraded due to heterogeneous reactions. Obtaining accurately the heterogeneous reaction rate is a complex task. In this work, as explained in Section 2.4, the heterogeneous reactions are accounted for using thermochemical tables. Considering the degradation of the material due to pyrolysis and heterogeneous reactions [8], the solid mass conservation equation becomes

$$\frac{\partial(\rho_s \epsilon_s)}{\partial t} = \frac{\partial(\rho_m \epsilon_m + \rho_f \epsilon_f)}{\partial t} = -\Pi + \sum_{k=1}^{N_s} \epsilon_i \omega_i^{het}, \tag{2.5}$$

where the subscripts s, m and f correspond respectively to the solid phase, the resin (matrix) and the carbon fibers. ω_i^{het} stands for the heterogeneous reaction rate of the gaseous species i.

2.2.2 Momentum conservation equation

The momentum conservation equation allows to compute the average gas velocity. The equation is derived from the volume averaged Navier-Stokes equation described in detail by Schrooyen in [6]. It can be written as follows

$$\underbrace{\frac{\partial\left(\epsilon_g \rho_g \boldsymbol{v}_g\right)}{\partial t}}_{\text{Conservative term}} + \underbrace{\nabla \cdot \left(\epsilon_g \rho_g \boldsymbol{v}_g \boldsymbol{v}_g\right)}_{\text{Convective term}} = \underbrace{-\epsilon_g \nabla P}_{\text{Pressure term}} + \underbrace{\nabla \cdot \underline{\underline{\boldsymbol{\tau}}}}_{\text{Viscous term}} + \underbrace{\frac{\mu}{\kappa} \epsilon_g^2 \boldsymbol{v}_g}_{\text{Drag term}}, \tag{2.6}$$

where P is pressure field, $\underline{\underline{\boldsymbol{\tau}}}$ is the second order viscous stress tensor, μ is the dynamic viscosity, and κ is the permeability of the porous medium.

The gas velocity is thus depend on the pressure gradient but also viscous and a drag effects. Following [46], the second order viscous stress tensor can be expressed as

$$\underline{\underline{\boldsymbol{\tau}}} = \mu \left(\nabla \left(\epsilon_g \boldsymbol{v}_g \right) + \nabla \left(\epsilon_g \boldsymbol{v}_g \right)^T - \frac{2}{3} \nabla \cdot \left(\epsilon_g \boldsymbol{v}_g \right) \underline{\underline{\boldsymbol{I}}} \right), \tag{2.7}$$

where $\underline{\underline{\boldsymbol{I}}}$ is the identity second order tensor.

Concerning the drag term, it corresponds to the drag imposed by the material when the gas percolates through the pores. Whitaker [47] proposed to model this term as given in Eq. (2.6).

Equation Eq. (2.6) can be simplified by dividing each side by the volume fraction ϵ_g [6]. The equation is thus reduced to

$$\frac{\partial \left(\rho_g \boldsymbol{v}_g \right)}{\partial t} + \nabla \cdot \left(\rho_g \boldsymbol{v}_g \boldsymbol{v}_g \right) = -\nabla P + \nabla \cdot \underline{\underline{\boldsymbol{\tau_g}}} + \frac{\mu}{\kappa} \epsilon_g \boldsymbol{v}_g, \tag{2.8}$$

where $\underline{\underline{\boldsymbol{\tau_g}}}$ is the second order viscous stress tensor (see Eq. (2.7)) divided by ϵ_g.

Eq. (2.8) is the equation implemented in Argo [6]. This equation allows to compute the average gas velocity with a high fidelity considering both the viscous and drag effects.

Note that the pyrolysis gas percolates through the pores at a relatively low velocity. Therefore, in models with a lower level of fidelity (type II), they assume that the gases behave as a creeping (Stokes) flow [8]. In this case, Eq. (2.8) degenerates into Darcy's law, and the average velocity is directly computed as follows

$$\boldsymbol{v}_g = -\frac{\kappa}{\mu_g \epsilon_g} \nabla P. \tag{2.9}$$

2.2.3 Energy conservation equation

To derive the energy conservation equation, it can be assumed that the solid and the gas phase are in thermal equilibrium. As explained by Puiroux et al. in [48], this assumption is valid if the Peclet number for the heat diffusion through the porous medium is small. The expression of the Peclet number is given by

$$Pe = \frac{\epsilon_g v_g \rho_g c_{p,g} L}{k}, \tag{2.10}$$

where $c_{p,g}$ is the specific heat of the gas mixture, L is the characteristic length, and k is the thermal conductivity. Looking at Eq. (2.10) and, following the development from Schrooyen in [6], the Peclet number can be considered to be small since the gas velocity is relatively low (as shown in the further sections, the order of magnitude for the pyrolysis gas velocity is about $1[m/s]$), and the material pores are small ($< 100[\mu m]$).

Thanks to the thermal equilibrium assumption, there is only one energy conservation equation which is equal to

$$\underbrace{\frac{\partial \left(\rho_a e_a \right)}{\partial t}}_{\text{Term I}} + \underbrace{\nabla \cdot \left(\epsilon_g \boldsymbol{v_g} \rho_g h_g \right)}_{\text{Term II}} = \underbrace{\nabla \cdot \left(k \nabla T \right)}_{\text{Term III}} + \underbrace{\frac{\mu_g}{\kappa} \epsilon_g \left(\boldsymbol{v_g} \cdot \boldsymbol{v_g} \right)}_{\text{Term IV}}. \tag{2.11}$$

The different terms in Eq. (2.11) correspond to:

Term I

The total storage energy of the ablative material. It includes the energy of the pyrolysis gas, the carbon fibers, and the matrix. The total energy is simply the sum of the energy of those three components

$$\rho_a e_a = \epsilon_g \rho_g e_g + \epsilon_f \rho_f e_f + \epsilon_m \rho_m e_m, \tag{2.12}$$

where e is the specific thermal energy, and the subscripts a, g, f and m refer to the ablative material (including the gas), the pyrolysis gas, the carbon fibers, and the matrix.

Term II

The energy convected by the pyrolysis gases. In this term, h_g corresponds to the enthalpy of the pyrolysis gases. It is the sum of the enthalpy of each gaseous species in the mixture h_i weighted by their respective mass fraction y_i,

$$h_g(T) = \sum_{i=1}^{N_s} y_i h_i(T). \tag{2.13}$$

The enthalpy of each gaseous species i can be separated in a chemical formation enthalpy $h^0_{f,i}$ and a sensible enthalpy. The formation enthalpy is defined at a particular temperature T_0 and the sensible enthalpy depends on the actual temperature and the heat capacity of the species $c_{p,i}$

$$h_i(T) = \underbrace{h^0_{f,i}}_{\substack{\text{Formation} \\ \text{enthalpy}}} + \underbrace{\int_{T_0}^{T} c_{pi} dT}_{\substack{\text{Sensible} \\ \text{enthalpy}}}. \tag{2.14}$$

Term III

The heat transferred by conduction. This is classically modeled by Fourier's law. k is the effective conductivity that includes the conduction in the solid and in the gas. To find the properties of the material, for example, the thermal conductivity, a common approach [6] is to make an interpolation based on the virgin and char material values,

$$k_s = \psi_v k_v + (1 - \psi_v) k_c. \tag{2.15}$$

In Eq. (2.15), k_s, k_v and k_c are respectively the thermal conductivity of the solid phase, the virgin and the charred material. ψ_v is the fraction of virgin material that remains at a particular state of the decomposition.

Note that for high fidelity level models (type III), the conductivity is expressed as a second-order tensor $\underline{\underline{\boldsymbol{k}}}$ to take into account the anisotropy of the material.

Term IV

The energy dissipated by the viscous effects. In most cases, this term is small compared to the heat transferred by conduction. Therefore, this term is often neglected (in type I and II models) and Eq. (2.11) is reduced to

$$\frac{\partial (\rho_a e_a)}{\partial t} + \nabla \cdot (\epsilon_g \boldsymbol{v_g} \rho_g h_g) = \nabla \cdot (k \nabla T). \tag{2.16}$$

2.3 Boundary conditions

As explained in Section 1.2.3, there are many interactions between the material and the flow. The in-depth thermal response of the material is strongly dependent on the phenomena that occur in the boundary layer. Two different approaches are used to model the boundary conditions between the boundary layer and the ablative material:

- The properties of the flow in the boundary layer are computed thanks to a CFD software, and then the information is exchanged at the interface with the material. As explained in Section 1.3.2, there can be either two separate tools for the flow and the material (weak coupling [22, 23]) or a unified tool (strong coupling [6, 26]).
- The properties of the boundary layer are modeled using transfer coefficients [28, 49]. Those transfer coefficients are computed thanks to simplified flowfield simulations and the surface conditions (e.g. the convective heat flux) are found thanks to semi-empirical relations. Mass and energy balance are used to computed the mass and heat transfer at the surface.

In this work, the second approach is used; surface mass and energy balance are implemented as boundary conditions.

2.3.1 Surface mass balance

To solve the mass balance at the interface between the boundary layer and the ablative material, the first step is to attach a control volume to the receding surface. It is essential to notice here that the surface will move due to the ablation of the material. Then, the fluxes of chemical elements k entering and leaving the control volume are considered. Fig. 2.1 shows a sketch of the control volume and the different mass fluxes.

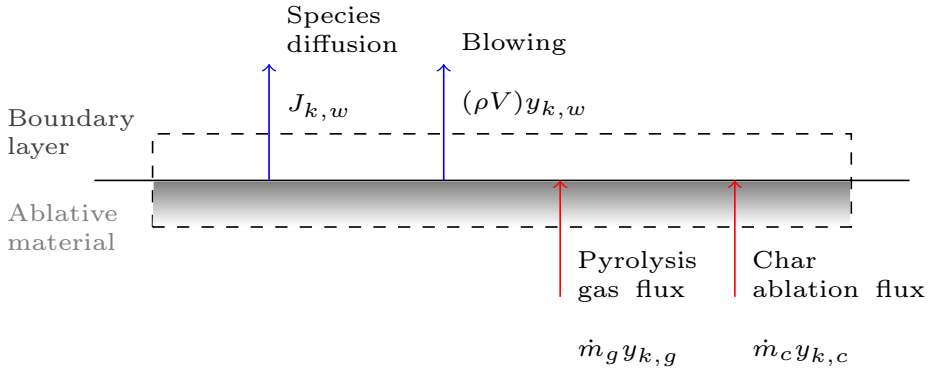

Fig. 2.1: Sketch of the mass balance with the mass fluxes at the interface between the ablative material and the boundary layer. Sketch based on a figures from Schrooyen [6] and Bianchi [10].

In this work, spallation (mechanical ablation) is neglected; hence as depicted in Fig. 2.1 the surface mass balance of an element k is given by

$$J_{k,w} + (\rho V)y_{k,w} = \dot{m}_g y_{k,g} + \dot{m}_c y_{k,c}, \tag{2.17}$$

where J stands for the diffusive flux, y is the mass fraction, and the subscripts w, g and c correspond respectively to the quantities at the wall, in the pyrolysis gas, and in the char.

$\dot{m}_g$ corresponds to the pyrolysis gas mass flow rate. It can be directly computed thanks to the gaseous phase mass conservation equation Eq. (2.1) (which allows to compute the gas mass density ρ_g) and the momentum conservation equation Eq. (2.6) (which provides the gas velocity v_g). After computing those quantities, it is straightforward to obtain the mass flow rate of the pyrolysis gas

$$\dot{m}_g = \rho_g v_g. \tag{2.18}$$

$\dot{m}_c$ is the char ablation products blowing rate. This term includes the different gaseous species produced by the heterogeneous reactions at the surface (see Section 1.2.2). Evaluating this term is complex since it depends on many thermal and chemical properties at the wall. Therefore, Section 2.4 is fully dedicated to explain how is the ablation rate computed.

ρV stands for the gross blowing rate. It corresponds to the mass flux of pyrolysis gas and ablation products, which will blow and inject the elements at the wall into the boundary layer (outside the control volume).

If all the chemical elements k are summed, the diffusion term vanishes, and the relative mass fractions sum to 1 in each phase

$$\sum_k y_{k,w} = 1; \sum_k y_{k,g} = 1; \sum_k y_{k,c} = 1. \tag{2.19}$$

In this case, Eq. (2.17) can be simplified and it is reduced to

$$\rho V = \dot{m}_g + \dot{m}_c. \tag{2.20}$$

2.3.2 Surface energy balance

Surface energy balance is used to compute the heat transfer at the interface between the boundary layer and the material. The method is quite similar to the one explained for the mass balance. A control volume is attached to the receding surface, and the energy fluxes entering and leaving the control volume are considered. To illustrate the following explanations, a sketch of the energy balance is shown in Fig. 2.2

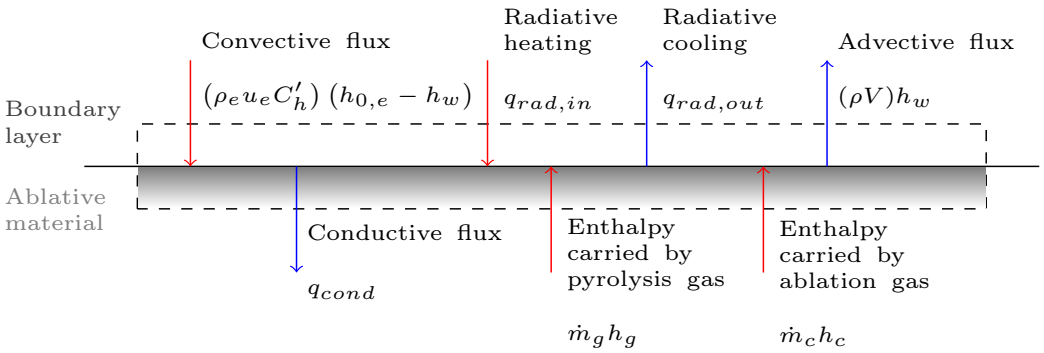

Fig. 2.2: Sketch of the energy balance at the interface between the ablative material and the boundary layer. Sketch based on figures from Schrooyen [6] and Bianchi [10].

The energy fluxes involved in the energy balance are described in detail hereafter.

Convective flux

As explained in Section 1.2.2, the surface of the ablative material is heated by convection of the high enthalpy flow from the boundary layer. The convective flux (q_{conv}) is generally provided by CFD simulations. It is computed thanks to the energy conservation equation in the boundary layer, considering a steady-state and laminar flow regime. As explained in detail by Bianchi [10], if the Prandtl (Pr) and the Lewis number (Le) are unitary, the convective flux at the wall can be expressed in terms of a heat transfer coefficient, and the enthalpy difference across the flow in the boundary layer

$$q_{conv} = \rho_e u_e C_h (h_{0,e} - h_w), \tag{2.21}$$

where the subscripts e and w are the quantities at the edge of the boundary layer and at the wall. ρ_e and u_e are the mass density and flow velocity at the edge of the boundary layer. C_h is the dimensionless heat transfer coefficient (or Stanton number for heat transfer), h_w is the enthalpy at the wall, and $h_{0,e}$ corresponds to the total enthalpy at the edge of the boundary layer (including the kinetic energy of the flow)

$$h_{0,e} = h_e + \frac{u_e^2}{2}. \tag{2.22}$$

Using the Reynolds analogy [10], the Stanton number can be expressed in terms of the skin friction coefficient C_f

$$C_h = Pr^{-\frac{2}{3}} \frac{C_f}{2}. \tag{2.23}$$

Moreover, a relation can be made between the heat and mass Stanton number (C_m) using the Chilton-Colburn relation

$$C_m = C_h (Le)^{\frac{2}{3}}. \tag{2.24}$$

Note that Eq. (2.21) is valid only if $Pr = Le = 1$. If the Prandtl is non-unitary, the total enthalpy at the edge of the boundary layer is replaced by a recovery enthalpy $h_{r,e}$

$$h_{r,e} = h_e + r_c \frac{u_e^2}{2}, \tag{2.25}$$

where r_c is the recovery factor which is given by

$$\begin{cases} r_c \approx \sqrt{Pr} & \text{for a laminar boundary layer} \\ r_c \approx \mathrm{Pr}^{\frac{1}{3}} & \text{for a turbulent boundary layer} \end{cases}. \tag{2.26}$$

If the Lewis is non-unitary, an additional term is added, in Eq. (2.21), to account for the enthalpy carried due to the diffusion of the chemical elements. The general expression for the convective flux is written as

$$q_{conv} = \rho_e u_e C_h \left(h_{r,e} - h_w\right) + \rho_e u_e C_m \sum_k \left(y_{k,e} - y_{k,w}\right) h_{k,w}. \tag{2.27}$$

The term on the right-end side is the enthalpy transported by the diffusion of each element k and y is the mass fraction.

The blowing of the pyrolysis gas and the ablation gas in the boundary layer will induce a blocking effect of the convective flux. A common practice to account for this effect is to correct the Stanton number as follows [50]

$$C'_h = C_h \left(\frac{\ln(1 + 2\iota B')}{2\iota B'} \right), \tag{2.28}$$

where ι is a scaling factor depending on the flow regime; it is taken equal to 0.5 for a laminar flow regime. B' is the dimensionless mass flow rate which is computed as follows

$$B' = B'_g + B'_{c'} \text{ with } B'_g = \frac{\dot{m}_g}{\rho_e u_e C_m}, \text{ and } B'_c = \frac{\dot{m}_c}{\rho_e u_e C_m}, \tag{2.29}$$

where B'_g is the dimensionless pyrolysis gas blowing rate, it can be computed directly thanks to Eq. (2.18) and knowing the mass transfer coefficient. Concerning B'_c, it is the dimensionless ablation blowing rate. It is tabulated in thermochemical tables, and it depends on the temperature, the pressure, and the pyrolysis gas blowing rate. Detail about the ablation rate and the thermochemical tables are given in Section 2.4.

Radiative heating

The excitation/de-excitation of the electronic population in the shock layer will induce radiation and hence contribute to the heat load (see Section 1.2.2). This radiative heating term ($q_{rad,in}$) should also be provided by CFD simulations. However, according to Potter [7], it is extremely complex to model. The radiative heating depends on different parameters, such as the electromagnetic spectrum distribution or the internal state populations of the chemical species. Therefore, in this work, the test cases studied do not consider radiative heating.

Radiative cooling

The surface of the ablative material will reach high temperatures (up to 3000[K]), and it has a high emissivity (for example, 0.9 and 0.8 for charred and virgin TACOT). Therefore, the surface of the ablative material will cool down by re-radiating energy according to the Stefan-Boltzmann law

$$q_{rad,out} = \sigma \xi ({T_w}^4 - {T_\infty}^4), \tag{2.30}$$

where σ corresponds to the Stefan-Boltzmann constant ($\approx 5.67e^{-4}[W/(m^2K^4)]$), ξ is the surface emissivity, T_∞ is the infinite temperature and T_w is the temperature at the surface (at the wall).

Advective flux

The blowing of pyrolysis and ablation gas will transport away the enthalpy of the gaseous species from the wall to the boundary layer. This advective flux can be expressed as

$$q_{adv} = (\dot{m}_g + \dot{m}_c) h_w. \tag{2.31}$$

If an overall gas is considered, thanks to the surface mass balance (Eq. (2.20)), the advective flux can be written with respect to a gross blowing rate ρV

$$q_{adv} = (\rho V) h_w. \tag{2.32}$$

Enthalpy carried by pyrolysis and ablation gas

The pyrolysis gas will percolate through the porous material and be injected into the boundary layer. The enthalpy of the pyrolysis gas will be carried towards the interface at a rate $\dot{m}_g h_g$. Similarly, the energy contained in the char will be transported away (due to the heterogeneous reactions) at a rate $\dot{m}_c h_c$.

Conductive flux

The energy is transported inside the solid by thermal conduction. As depicted in Fig. 2.2, if the different energy fluxes are gathered, and surface energy balance is considered, the conductive flux can be expressed by

$$q_{cond} = (\rho_e u_e C'_h)\,(h_{0,e} - h_w) + \dot{m}_g h_g + \dot{m}_c h_c + q_{rad,in} - q_{rad,out} - (\rho V) h_w. \tag{2.33}$$

2.4 Ablation rate and thermochemistry

As explained in Section 1.2.2, in a high heating environment, a charring ablative material degrades by two phenomena: pyrolysis and erosion/ablation. During pyrolysis, the resin is transformed into gases and char. Then, the remaining char and the carbon fibers are eroded due to heterogeneous reactions, sublimation, or mechanical ablation (spallation). There are two types of ablation which are surface and volume ablation. As a reminder, in surface ablation, the material degrades and loses mass mainly on the surface. In volume ablation, the flow from the boundary layer percolates within the material and erodes the fibers in-depth. The objective of this section is to present the different approaches used to model and compute the ablation rate $\dot{m}_c$. It is essential to evaluate the ablation rate since it is needed to compute the surface mass and energy balance. Moreover, estimating the total recession is crucial for designing a TPS for a given mission.

To model the ablation rate, several methods with different levels of fidelity are available [51]. Some empirical models estimate the ablation rate as a function of the surface temperature only. In this case, experimental data are used to correlate the recession and the surface temperature for a particular pressure range. Another common approach is the $Q*$ model. In this model, the ablation rate is computed as follows

$$\dot{m}_c = \frac{q_{conv}}{Q^*} \quad \text{for } T_w \geq T_{abl}, \tag{2.34}$$

where q_{conv} is the convective heat flux (described in Section 2.3.2), Q^* is the effective heat of ablation, and T_{abl} is the theoretical surface temperature at which the surface starts to ablate. The Q^* model provides a good approximation of the ablation rate when a steady-state recession can be assumed. On the other hand, the main drawback is that the temperature history cannot be obtained.

The most general method to predict the ablation rate is the thermochemical ablation model [27, 52, 53]. In this approach, the ablation rate is predicted, assuming thermodynamic equilibrium between the ablative material and the flow. The results of this model provide thermochemical tables which relate the ablation rate to the temperature, the pressure, and the pyrolysis gas blowing rate

$$B'_c = \mathcal{F}(T_w, p_w, B'_g). \tag{2.35}$$

Note that the pyrolysis gas and the ablation blowing rate are expressed with the dimensionless variables B'_g and B'_c described in Eq. (2.29). The tables are generated for a specific ablative material, such as PICA, and a specific atmospheric composition, such as air. The methodology to obtain those tables is described in Section 2.4.1.

Once the B'_c is obtained from the thermochemical tables, the dimensional ablation rate and the recession velocity can directly be computed as follows

$$\dot{m}_c = \rho_e u_e C_m B'_c, \tag{2.36}$$

$$\dot{S} = \frac{\dot{m}_c}{\rho_s}, \tag{2.37}$$

where $\dot{S}$ is the recession velocity and ρ_s is the solid mass density.

The thermochemical ablation model is used in this work since it provides a good approximation of the ablation rate. The main advantage of this model is that, once the tables are generated, it is applicable for various heating conditions, and it significantly reduces the computational cost. Nevertheless, this method does not consider volume ablation, but only surface ablation, and a thermochemical equilibrium is assumed. For this reason, the ablation rate is often overestimated with the thermochemical tables.

Finally, note that in Argo, a model was originally implemented to obtain the heterogeneous reactions and the ablation rate in an accurate manner [6]. This model computes the heterogeneous reactions using finite-rate chemistry. It considers the reactions (oxidation, nitridation) between the carbon fibers and the species in the boundary layer (see Section 1.2.2). This accurate method considers a strong coupling approach between the material and the flow. Therefore, this model will not be considered in this work dedicated to investigating a material solver only.

2.4.1 Thermochemical tables

To generate the thermochemical tables, a set of equations is used to derive a relation between the ablation rate and the thermochemical properties [10].

A first equation can be obtained based on the mass balance for each chemical element k given in Eq. (2.17). If the Prandtl and the Lewis number are assumed unitary, and if equal diffusion coefficients are considered, the diffusive flux can be expressed in terms of a mass transfer coefficient and a mass fraction difference across the flow in the boundary layer

$$\rho_e u_e C_m (y_{k,w} - y_{k,e}) + (\rho V) y_{k,w} = \dot{m}_g y_{k,g} + \dot{m}_c y_{k,c}. \tag{2.38}$$

If Eq. (2.38) is divided on each side by $\rho_e u_e C_m$, the mass balance equation can be written in terms of the dimensionless blowing rates

$$(1 + B') y_{k,w} = B'_g y_{k,g} + B'_c y_{k,c} + y_{k,e}. \tag{2.39}$$

The mass fraction of the element k at the wall can therefore be expressed as

$$y_{k,w} = \frac{B'_g y_{k,g} + B'_c y_{k,c} + y_{k,e}}{1 + B'}. \tag{2.40}$$

The second step to derive the thermochemical tables is to assume chemical equilibrium between the gaseous species. To do so, the formation reactions of each species A_i from the chemical elements A_k are considered. Those chemical formation reactions can be written as

$$\sum_k \nu_{i,k} A_k \rightleftharpoons A_i, \tag{2.41}$$

where $\nu_{i,k}$ is the number of atomic elements k in a molecule of species i. The chemical equilibrium corresponding to Eq. (2.41) can be expressed as

$$\sum_k \nu_{i,k} \ln(p_k) - \ln(p_i) - \ln(K_i(T_w)) = 0, \tag{2.42}$$

where p_k and p_i are respectively the partial pressure of the element k and the species i. K_i is the equilibrium constant for the formation reaction related to species i. Note that the equilibrium constant depends on the temperature at the wall T_w.

In the case where A_i is a solid species, equation Eq. (2.43) is reduced to

$$\sum_k \nu_{i,k} \ln(p_k) - \ln(K_i(T_w)) = 0. \tag{2.43}$$

Moreover, thanks to Dalton's law, the total pressure can be expressed in terms of the partial pressures

$$p_w = \sum_i p_i. \tag{2.44}$$

Finally, the mass fraction of the element k at the wall can be expressed as

$$y_{w,k} = \frac{W_k}{p_w W} \sum_i \nu_{ki} p_i, \tag{2.45}$$

where W is the molecular weight of the element k and W is the average molecular weight of the overall gas.

The set of equation is closed thanks to Eq. (2.40) and Eq. (2.43) to Eq. (2.45). Based on those equations, the dimensionless ablation rate can be computed when the following properties are specified: the wall pressure p_w, the wall temperature T_w, and the pyrolysis blowing rate B'_g. The thermochemical tables can be generated for a particular ablative material and atmospheric molecular composition.

Fig. 2.3 shows the B'_c according to the wall temperature for a wall pressure of $1[atm]$ and different B'_g from 0.001 up to 10. The material considered here is TACOT and the atmosphere is air ($X_{N_2} \approx 79\%$, $X_{O_2} \approx 21\%$). Note that the thermochemical tables used to make this figure comes from the spreadsheet of test cases 1 and 2 from Lachaud et al. [33, 44].

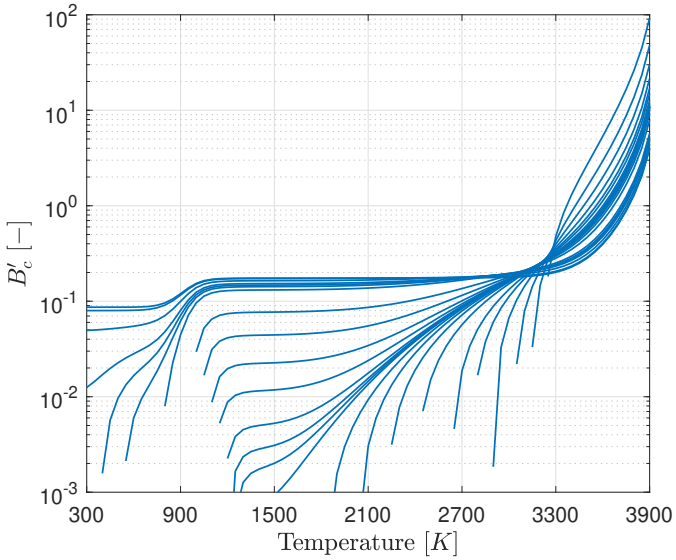

Fig. 2.3: B'_c according to the temperature for a pressure of 1$[atm]$ and different B'_g (0.001 $\rightarrow$ 10).

2.5 Conclusion

The constitutive equations and the boundary conditions presented in this section allow to model the in-depth thermal response of an ablative material submitted to a high enthalpy flow. The constitutive equations were already implemented in Argo, and the boundary conditions (mass and energy balance) have been added during this work. Transfer coefficients are used to model the heat and mass exchanges at the interface between the boundary layer and the material. The energy balance allows to compute the conductive heat flux in the material. As explained, in Section 1.2.2, due to the temperature rise, the ablative material degrades due to pyrolysis and ablation. To model the pyrolysis decomposition of the resin, Arrhenius laws and the three-components decomposition model from Goldstein [43] are used. Concerning ablation, it is accounted for using B' thermochemical tables. Thanks to those tables, the ablation rate, and the recession velocity can be obtained.

3 Recession modeling

3.1 Review of immersed interface methods

As explained in Section 1.2.2, the charred surface of the ablative material will degrade due to heterogeneous reactions, phase changes, and mechanical ablation. Therefore, the material will recede, and the boundary between the solid and the flow will move. For this reason, taking recession into account is a complex task because the computational domain changes when the material degrades.

Different immersed numerical methods exist to deal with this moving boundary problem. Two main techniques can be distinguished: interface tracking and interface capturing. In the interface tracking method, the mesh follows the interface, and it is updated depending on the recession. In the interface capturing technique, the mesh does not have to be tied to the interface and to follow it. Fig. 3.1 shows a comparison between the interface tracking and capturing techniques [6]. For the interface tracking (Fig. 3.1a), it can be observed that the mesh is modified to stay conform to the interface. On the other hand, for interface capturing (Fig. 3.1b), the interface is captured, and it passes through the elements. This section presents an overview of some interface tracking and capturing techniques. Then in Section 3.2 the focus is placed on the immersed level-set method implemented in Argo.

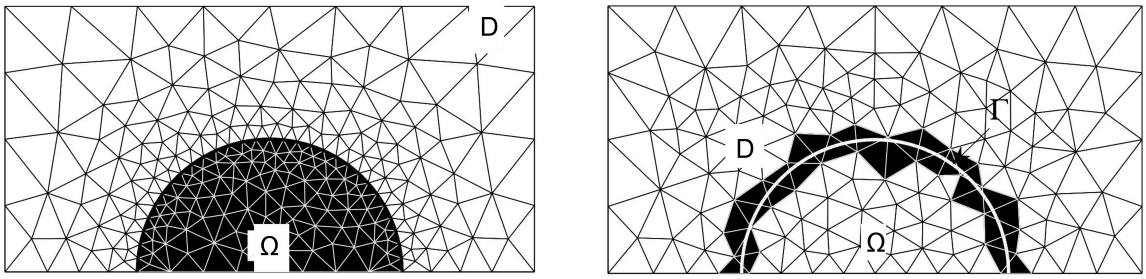

(a) Interface tracking (b) Interface capturing

Fig. 3.1: Overview and comparison between interface tracking and capturing techniques. Figure modified from Schrooyen [6].

3.1.1 Interface tracking

The interface tracking method is widely used to model the recession of ablative materials. Various techniques can be found in the literature, but they can be classified into two main categories:

- In the first category, the number of nodes in the mesh is constant, and the length of the domain is adjusted to account for recession. In this case, Landau coordinates are used to perform the transformation from one configuration to another.
- In the second approach, the number of nodes in the domain is not constant, and the mesh is modified close to a boundary. A first method consists in changing the position of the first node when recession is sufficient [54]. Another technique is to attach the mesh to the moving surface and remove the last node when the recession length is higher than an element [50]. It has been demonstrated that it is more efficient to remove the last node because it leads to less oscillatory results.

In most interface tracking methods, the mesh will move due to recession and therefore the domain will change. When moving mesh methods are used, the system of equations presented is Section 2 must be rewrite in a moving coordinate system. This system of coordinate is attached to the receding surface. For example, the energy conservation equation Eq. (2.16) (in one-dimension), becomes

$$\frac{\partial\left(\rho_a e_a\right)}{\partial t}+\frac{\partial\left(\epsilon_g v_g \rho_g h_g\right)}{\partial x}=\frac{\partial}{\partial x}\left(k\frac{\partial T}{\partial x}\right)+\dot{S}\frac{\partial\left(\rho_a e_a\right)}{\partial x}, \tag{3.1}$$

where the second term on the right-end side is an additional term that corresponds to the energy convected due to the coordinate system movement. It depends on $\dot{S}$ which is the recession velocity.

The interface tracking technique is best suited for simple one-dimensional problems. When multi-dimensional cases and complex shapes are considered, the method is often inadequate, and the interface capturing technique is preferred. There are two significant drawbacks of the interface tracking methods. First, the mesh will deform due to recession, which can degrade the mesh quality. On the other hand, the re-meshing and the geometry actualization can be complex and contribute to a high computational time.

3.1.2 Interface capturing

The advantage of the interface capturing method is that the mesh does not have to follow the interface. The interface can pass through the elements as shown in Fig. 3.1b and the structure of the mesh is not modified during the computation. To model the recession of ablative materials, this approach is thus much more efficient than interface tracking. In the literature, there are two widely used interface capturing methods: the Volume-of-Fluid (VOF) method [55], and the level-set method [56].

Volume-of-Fluid (VOF) method

In this method, the volume fraction of one phase is computed in each mesh element. The idea is to use a one-phase formulation to treat multi-phase problems [57]. To do so, a marker function χ is used, and as depicted in Fig. 3.2, it can be defined as follows

$$\chi=\begin{cases}1 & \text{when it is in the phase 1 (e.g solid, ablative material)}\\ 0 & \text{when it is in the phase 2 (e.g gas, boundary layer)}\end{cases}. \tag{3.2}$$

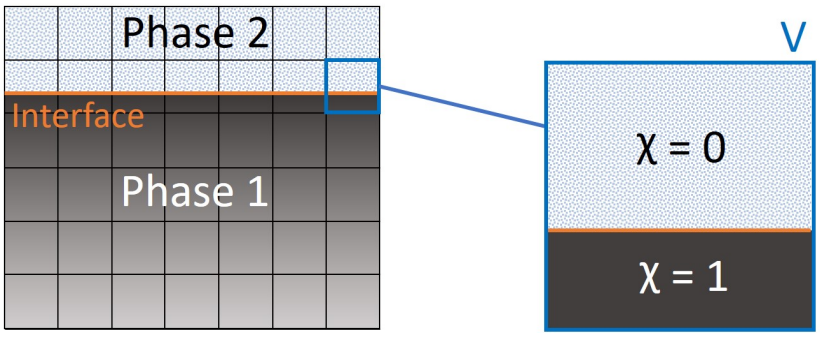

Fig. 3.2: Illustration of the VOF method and the marker function χ. Sketch inspired by [57].

The marker function allows to characterize the phase change in each mesh element. Note that, instead of having a complex set of equations for each phase, the equations can be gathered and expressed in terms of the marker function [57]. For example, the mass conservation equation is given by

$$\frac{\partial \rho}{\partial t} + \nabla \cdot (\rho \mathbf{u}) = 0 \quad \text{where} \quad \rho = \rho_1 + (\rho_1 - \rho_2)\chi, \tag{3.3}$$

where ρ_1 and ρ_2 are the mass density in phase 1 and phase 2.

Once the marker function is defined, a fraction variable C is computed in each volume element V (typically a mesh element) [57]

$$C = \frac{1}{V} \int_V \chi(\boldsymbol{x}, t) dV. \tag{3.4}$$

If $C = 1$, phase one fully occupies the element, and when $C = 0$, the element is filled with phase two. On the other hand, if $0 < C < 1$, the interface passes through the element, and both phases are present.

If the interface moves at a particular normal velocity V_n, the convection equation of the volume fraction is given by

$$\frac{\partial C}{\partial t} + V_n \|\nabla C\| = 0. \tag{3.5}$$

The advantage of the VOF method is that it ensures mass conservation [57]. The complex part of this approach is that the position of the interface is not explicitly provided. The interface must be retrieved thanks to reconstruction strategies, such as the PLIC method [58]. With the VOF method, it is complex to obtain a good topology at the interface. In the case of a sharp interface, there can be huge errors if the volume fraction is not solved accurately.

Level-set method

In the level-set method [56], instead of computing the volume fraction (like in the VOF method), an implicit field that defines the distance to the interface is solved. The advantage is that this field is smoother than the volume fraction, thus, it is easier to solve numerically. Moreover, with this method, it is straightforward to access to the interface topology. The level-set method is widely used in the literature to deal with immersed sharp interfaces. The level-set method is implemented in Argo, and it will be used in this work to model the recession. More detail about this method is given in Section 3.2.

3.2 Level-set method implemented in Argo

In Argo, a high order level-set method is implemented to treat multi-phase, and moving interface problems [59]. This immersed method is used in this work to model recession in an accurate manner. The interface between the ablative material and the flow moves due to recession, and the level-set method allows to deal with this moving boundary. The bases of this widely used method are explained in detail in this section and illustrated thanks to an example of immersed problem implemented in Argo.

3.2.1 Methodology and governing equations

In the level-set method, the interface Γ is represented by the zero iso-contour of an implicit level-set function ϕ [59, 56]. The interface Γ has a dimension of $d-1$ and ϕ is a d dimensional function. Note that they are both time dependent. As depicted in Fig. 3.3, based on the level-set value the domain is separated in different zones

$$\begin{cases} \phi(\boldsymbol{x},t) > 0 & \forall \boldsymbol{x} \in \Omega \backslash \Gamma \\ \phi(\boldsymbol{x},t) = 0 & \forall \boldsymbol{x} \in \Gamma \\ \phi(\boldsymbol{x},t) < 0 & \forall \boldsymbol{x} \in \mathrm{D} \backslash \Omega \end{cases}, \tag{3.6}$$

where $\boldsymbol{x}$ is the vector of coordinates, Ω corresponds to the solid domain (e.g. the ablative material), and D is the design domain (the entire mesh).

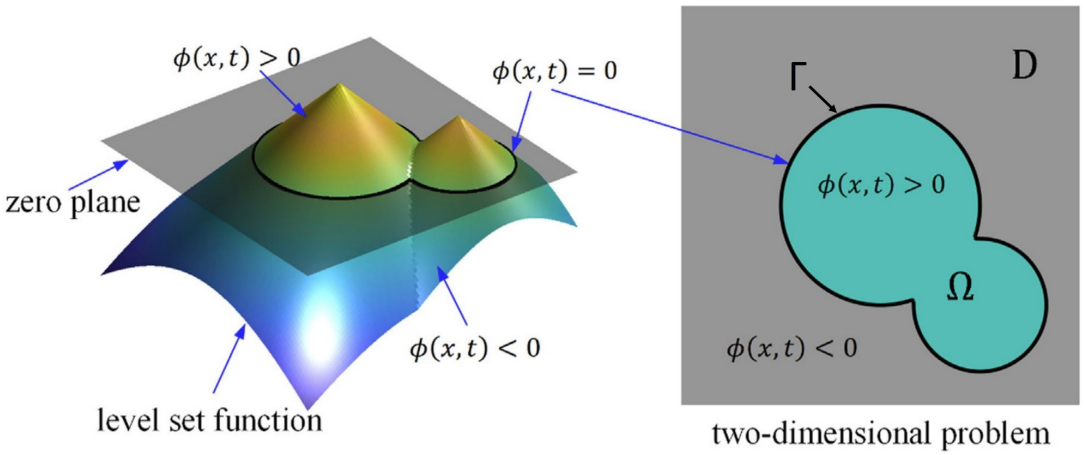

Fig. 3.3: Illustration of the level-set method for a two-dimensional problem. Figure from [56]

As explained in [59], once the interface is known, the level-set function is generally defined in terms of a signed distance function. The distance from the interface Γ is computed for each point $\boldsymbol{x}$ as follows

$$\mathrm{dist}(\boldsymbol{x},\Gamma) = \min \|\boldsymbol{x} - \boldsymbol{x}_{\Gamma,\mathrm{cp}}\|, \tag{3.7}$$

where $\boldsymbol{x}_{\Gamma,cp}(\boldsymbol{x},t) \in \Gamma$ is the point on the interface which is the closest from $\boldsymbol{x}$. Based on the distance function, the level-set function is given by

$$\phi(\boldsymbol{x},t) = \begin{cases} \mathrm{dist}(\boldsymbol{x},\Gamma) & \forall \boldsymbol{x} \in \Omega \backslash \Gamma \\ 0 & \forall \boldsymbol{x} \in \Gamma \\ -\mathrm{dist}(\boldsymbol{x},\Gamma) & \forall \boldsymbol{x} \in \mathrm{D} \backslash \Omega \end{cases}. \tag{3.8}$$

Expressing the level-set function in terms of a distance function is advantageous. Indeed, a particularity of the distance function is that it is everywhere differentiable, and its gradient satisfies the eikonal equation [59]. Therefore the following relation is valid for every $\boldsymbol{x}$ coordinates in the domain

$$\|\nabla \phi(\boldsymbol{x})\| = \|\nabla \,\mathrm{dist}(\boldsymbol{x},\Gamma)\| = 1. \tag{3.9}$$

To demonstrate this relation, the classical distance function in two-dimensions can be taken as example

$$d(x,y) = \sqrt{x^2+y^2}, \tag{3.10}$$

$$\nabla d = \left[\frac{x}{\sqrt{x^2+y^2}}, \frac{y}{\sqrt{x^2+y^2}}\right], \tag{3.11}$$

$$\|\nabla d\| = \sqrt{\frac{x^2}{x^2+y^2} + \frac{y^2}{x^2+y^2}} = 1. \tag{3.12}$$

In the case of a moving interface, the level-set function must be updated. To do so and to obtain the position of the interface, the following advection equation [56] is solved

$$\frac{\partial \phi}{\partial t} + V_n \|\nabla \phi\| = 0, \tag{3.13}$$

where V_n is the normal advection velocity. It can be computed as follows

$$V_n = \boldsymbol{V} \cdot \boldsymbol{n} = \boldsymbol{V} \cdot \left(\frac{\nabla \phi(\boldsymbol{x},t)}{\|\nabla \phi(\boldsymbol{x},t)\|}\right), \tag{3.14}$$

where $\boldsymbol{V}$ is the extended advection velocity and $\boldsymbol{n}$ is the normal vector.

Note that due to advection, the interesting distance property, defined in Eq. (3.9), can be lost [59]. This can be due to two principal reasons. The first problem is that the level-set function can become too flat to find the zero level set. On the other hand, the level set gradient can become too steep, leading to instabilities. To deal with those problems, re-initialization is commonly used to retrieve the distance property.

3.2.2 Example in Argo

The high order level-set method implemented in Argo [59] is used to model the recession of the material. This efficient immersed method accurately captures the interface between the ablative material and the boundary layer. In Argo, there are two steps to model recession thanks to the level-set method.

1. The initial iso-0 level-set must be provided. In other words, the topology of the interface Γ must be specified at time $t = 0[s]$. Once the zero level-set is know, the level-set function is computed using the distance function (see Eq. (3.8)). The interface can be defined either by using an analytical expression or by creating a specific mesh for the interface.
2. The second step is to define the normal advection velocity of the interface. This allows to solve the advection equation given in Eq. (3.13). In this work, the normal velocity of the interface corresponds to the recession velocity. The recession velocity depends on the ablation blowing rate and the material density; it can be computed directly thanks to Eq. (2.37).

Fig. 3.4 shows an example of immersed diffusive problem in Argo. The interface Γ (the iso-0 of the level set) can be observed. The interface passes through the mesh elements,

but it is not an issue in the level-set method (which is an interface capturing method). Note that, for the clarity of this example, the same interface as in Fig. 3.3 has been used.

The different zones are also depicted in the figure. It can be seen that when the level-set is positive ($\forall \boldsymbol{x} \in \Omega \backslash \Gamma$), the elements are taken into account in the computation. On the other hand, in the case of a negative level-set ($\forall \boldsymbol{x} \in \mathrm{D} \backslash \Omega$), the elements are not considered. It can be observed, in Fig. 3.4b, that the diffusion occurs only in the domain where the level-set is positive; the rest is not taken into account.

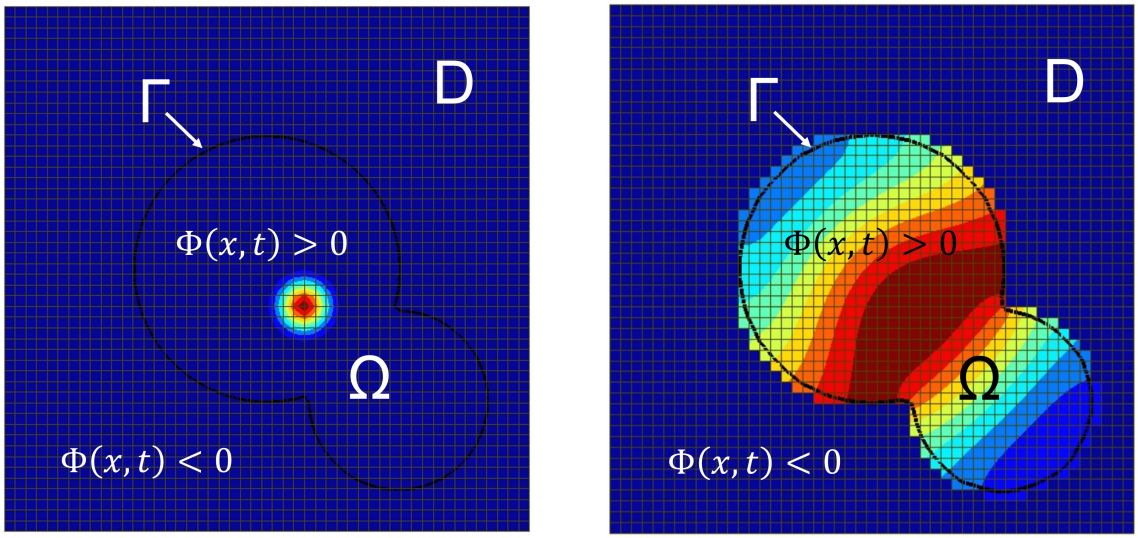

(a) $t = t_0$ (b) $t = t_1$

Fig. 3.4: Example of an immersed diffusive problem in Argo. The zero level-set and the different zones can be observed. Note that for clarity the same interface as in Fig. 3.3 as been used.

3.3 Conclusion

Due to the recession of the ablative material, the solid-gas interface moves, and it involves to deal with a moving boundary problem. In Argo, a high-order level-set interface capturing method is implemented. This method allows to accurately model the recession of the material by capturing the interface between the material and the flow. Compared to interface tracking methods, the main advantage is that no re-meshing is needed, and the mesh is not deformed when the interface moves. Moreover, it is easier to solve numerically than other interface capturing methods like the VOF method. In the level-set method, the evolution of the boundary is transformed in the update of the zero iso-contour of a level-set function. Fig. 3.4 shows that the level-set method implemented in Argo works well for an immersed diffusive problem. The following sections will demonstrate the abilities of the level-set method to model recession and deal with a moving interface.

4 Results and verification of the material response code

4.1 Introduction

The objective of this section is to verify (i) the implementation of the surface mass and energy balance and (ii) the recession modeling thanks to the level-set method and the B' thermochemical tables. The code is verified thanks to three different test cases proposed by Lachaud et al. [33, 44, 45] and the results are compared with state-of-the-art codes. The two first test cases are one-dimensional; they are dedicated to verify the constitutive equations, the surface mass and energy balance, and the recession modeling. The last test case is multi-dimensional; it will allow to demonstrate the ability of the material response code to treat multi-dimensional ablation problems.

The material used for the test cases is TACOT (Theoretical Ablative Composite for Open Testing) which is a theoretical material developed for code and model comparison. The properties of this material are publicly available [33, 44, 45], and it has thermochemical properties similar to current low-density ablators (such as PICA).

The code results are compared with PATO [28] which is a high fidelity tool used to implement and test new models (see Section 1.3.3). The in-depth thermal response, the mass blowing rates, the position of pyrolysis/char zone, and the recession will be compared to verify the material solver.

Before going further, it is important to understand that, for the test cases, the models implemented in Argo and PATO are not exactly the same. For this reason, the code results presented hereafter will slightly differ from the results obtained with PATO. There are two main differences between the models:

1. In this work, the homogeneous reactions between the different gaseous species are not considered. Note that homogeneous reactions are implemented in Argo but they were not taken into account because it is computationally expensive. In this work, the chemistry is thus assumed in a frozen state; the pyrolysis gas species will not react with each other or with the gaseous species present in the boundary layer.

   In PATO, for the test cases, homogeneous reactions were considered between the gaseous species, and the pyrolysis gas is assumed in chemical equilibrium. The composition of the overall pyrolysis gas will thus be different in this work and in PATO. Consequently, the pyrolysis gas properties such as the heat capacity c_p, the total enthalpy h_g, or the viscosity μ_g will also differ.

2. For the test cases, the multi-species diffusion model implemented in Argo and PATO is different. In this work, multi-component diffusion coefficients provided by Mutation++ are used. Mutation++ is a library developed at the von Karman Institute that provides accurate computation of thermodynamic and transport properties. The approach used in Argo is accurate since the coefficients are obtained thanks to Mutation++, based on collisional data [41]. Oppositely, in the test cases realized with PATO, equal diffusion coefficients have been used [33].

Those two main differences in the model will lead to discrepancies in the results. Indeed, in the test cases, the pyrolysis gas composition and the properties will not be the same using Argo or PATO. This will lead, for example, to a different thermal conductivity leading to differences in the in-depth thermal response.

4.2 One-dimensional test cases

4.2.1 Ablation test case 1 : Imposed surface temperature without recession

Description and objectives

In the first one-dimensional test case [33], a sample of TACOT of $5[cm]$ is heated for $1[min]$. The material is submitted, on one side, to a step of temperature of $1644[K]$, at atmospheric pressure. On the other side, an adiabatic and impermeable boundary condition is considered. Concerning the initial conditions, the temperature of the material is $298[K]$, and the pressure is equal to $101325[Pa]$. In this test case, recession is not taken into account.

The objective of this simple test case is to verify the constitutive equations implemented in Argo. Note that surface mass and energy balance, and recession modeling will be verified with the next test cases. In this section, the results for the in-depth thermal response will be analyzed and compared with the results obtained with PATO [28], and Echion [40, 41]. To get the temperature field of the material, numerical probes have been placed at different depths, respectively at a distance of $\{0, 2, 4, 8, 16, 50\}[mm]$ from the surface.

Results

Fig. 4.1a shows the temperature field for the test case 1 considering several species in the pyrolysis gas. The initial composition of the pyrolysis gas is given in Table 4.1. The results obtained with Argo (the symbols) are compared with those from PATO (the solid lines). It can be observed that there are discrepancies in the in-depth temperature. The temperature obtained with Argo is lower than the one from PATO. As explained in detail in Section 4.1, this is because the models implemented in Argo and PATO are not the same. In this work, the homogeneous reactions are not considered, and the model used in Argo for diffusion is more complex. Consequently, the composition of the gas mixture will not be the same, leading to different thermal and transport properties for the gas. The effective thermal conductivity k (see Eq. (2.11)) obtained with Argo is hence lower than the one obtained with PATO. This explains why the in-depth temperature is lower. Note that those discrepancies will also be present in the following test cases for the same reasons.

Table 4.1: Initial composition of the pyrolysis gas [33].

Species	C_6H_5OH	H_2O	CO	CH_4	H_2	C_6H_6	CO_2
Molar fraction	0.089	0.234	0.057	0.1	0.499	0.005	0.016
Mass fraction	0.458	0.23	0.088	0.087	0.055	0.044	0.038

If only C_6H_5OH is considered in the pyrolysis gas, the results for the temperature field for TACOT are shown in Fig. 4.1b. It is coherent to consider only C_6H_5OH because referring to Table 4.1, it is the species in the pyrolysis gas with the highest mass fraction. The results for the in-depth thermal response are compared between Argo (the symbols) and Echion (the dotted lines). In this case, since there is only one species, the gas composition is the same for both tests. Therefore, the thermal and transport properties of the gas are also equal. It can be observed in Fig. 4.1b that the results from Argo are in

good agreement with Echion. There is an average difference of 1.26% for the temperature at 60[s] (because the mesh resolution used in Echion and Argo are not the same).

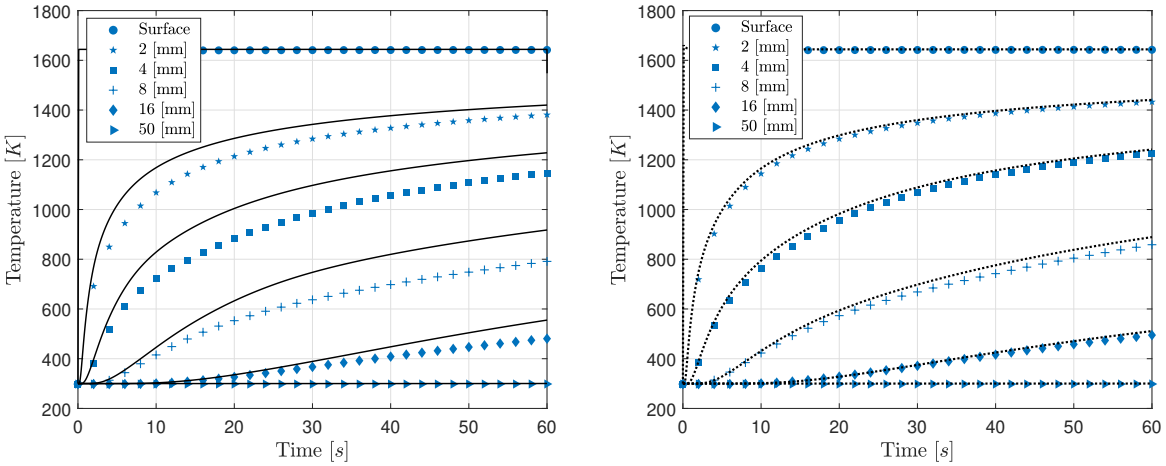

(a) Temperature field for TACOT considering several species in the pyrolysis gas Comparison between Argo and PATO[28].

(b) Temperature field for TACOT considering only C_6H_5OH in the pyrolysis gas. Comparison between Argo and Echion [40, 41].

Fig. 4.1: In-depth thermal response for TACOT submitted to an imposed surface-temperature without recession (Test case 1 [33]). The symbols are Argo results, the black solid and dotted lines are respectively PATO results and Echion results.

This first test case allowed to verify the constitutive equations implemented in Argo. If the same pyrolysis gas properties are considered, the Argo results for the in-depth thermal response are in good agreement with state-of-the-art codes (such as Echion).

4.2.2 Ablation test case 2.1 : Convective heat flux without recession

Description and objectives

In test cases 2.1 and 2.2 [44], the material properties are the same as in test case 1. The main difference with the first test case is that, at the surface, a convective boundary condition is considered instead of an imposed surface temperature. The material is heated on one side by a convective heat flux for 1[min], then cooled down for 1[min] by pure radiative cooling. On the other side, an adiabatic and impermeable boundary condition is used. For the initial conditions, $T_0 = 300[K]$ and $p_0 = 1[atm]$.

A sketch of the boundary conditions for test cases 2.1 and 2.2 is shown in Fig. 4.2. As explained in Section 2.3.2, the convective heat flux is expressed by Eq. (2.21). It depends on a heat transfer coefficient and the enthalpy difference across the flow in the boundary layer. The heat transfer coefficient $\rho_e u_e C_h$ and the enthalpy at the edge of the boundary layer $h_{0,e}$ are imposed and given in Table 4.2. Concerning the enthalpy at the wall h_w, it can be obtained thanks to the B' thermochemical tables provided in the test case spreadsheet [44]. It depends on the temperature at the wall T_w, the pressure at the wall p_w, and the dimensionless pyrolysis gas blowing rate B'_g. Note that a linear ramp of 0.1[s] is applied when the heat flux is applied or removed.

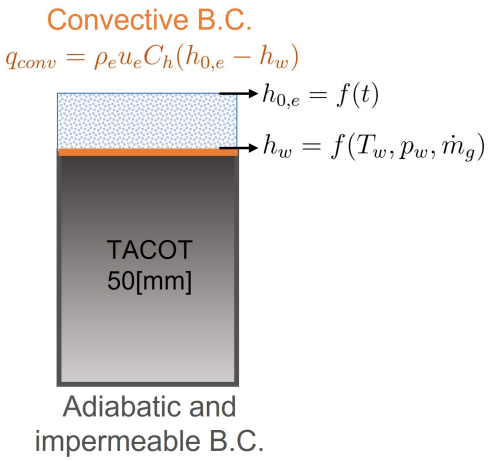

Fig. 4.2: Sketch of the boundary conditions used for the test cases 2.1 and 2.2.

Table 4.2: Properties of the boundary layer for the test cases 2.1 and 2.2 [44].

Time $[s]$	$\rho_e u_e C_h$ $[kg/(m^2 s)]$	$h_{0,e}$ $[J/kg]$	p_w $[Pa]$
0	0	0	101325
0.1	0.3	$1.5 \cdot 10^6$	101325
60	0.3	$1.5 \cdot 10^6$	101325
60.1	0	0	101325
120	0	0	101325

In test case 2.1, recession is not taken into account. The objective is to verify the implementation of the surface energy balance by comparing the results with PATO. Referring to Eq. (2.33), if the energy balance is correctly implemented, the conductive flux and the temperature at the surface should be correct.

Results

The temperature field for TACOT submitted to a convective heat flux is given in Fig. 4.3a. Note that several species have been considered in the pyrolysis gas (see Table 4.1). The first important observation that can be made is that the surface temperature is in good agreement with PATO. The difference between Argo and PATO for the surface temperature at $60[s]$ is 1.13%. Concerning the in-depth temperature, there are discrepancies with PATO. Again, as explained in detail in Section 4.1, this is because the models implemented in Argo and PATO are not the same. The transport and thermal properties of the gas mixture are thus different.

Fig. 4.3b shows the mass blowing rates (pyrolysis and char) and the position of the pyrolysis and char zone. The pyrolysis blowing rate computed with Argo is lower than the one from PATO. This difference in the results can be explained. As shown in Fig. 4.3a, the in-depth temperature is lower with Argo, so, referring to Eq. (2.4), the pyrolysis production rate will also be lower. Concerning the char blowing rate, it is equal to zero in this test case because recession is not considered.

The position of the pyrolysis and char zone can be obtained by looking at the mass density of the material. The zones start when the density reaches a certain threshold [44]. The threshold for the mass density at the beginning of the pyrolysis and char zone are given by definition as follows

$$\begin{aligned} \rho_{v,t} &= \rho_c + 0.98\,(\rho_v - \rho_c)\,, \\ \rho_{c,t} &= \rho_c + 0.02\,(\rho_v - \rho_c)\,, \end{aligned} \tag{4.1}$$

where ρ_v and ρ_c are the density of pure virgin material and pure char. $\rho_{v,t}$ and $\rho_{c,t}$ are the threshold value for the beginning of the pyrolysis and char zone.

It can be observed in Fig. 4.3b that the char zone starts at a depth of about $2.5[mm]$

and the pyrolysis zone at a depth of about 2$[cm]$. The results for the char zone are in good agreement with PATO, and for the pyrolysis zone there are slight discrepancies. The difference can also be explained by the fact that the computed in-depth temperature is lower with Argo. If the temperature is too low, the pyrolysis reaction does not start (see Table 2.1). With Argo, the depth at which the temperature is sufficient for the resin to pyrolyze is closer to the surface.

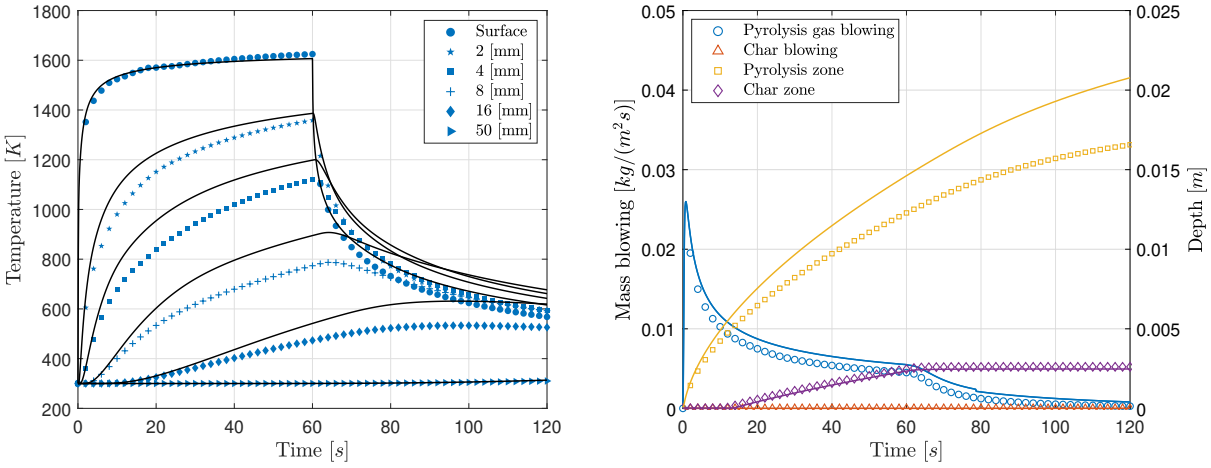

(a) Temperature field for TACOT

(b) Mass blowing rates, pyrolysis and char zone

Fig. 4.3: In-depth thermal response for TACOT submitted to a convective heat flux without recession (Test case 2.1 [44]). Comparison between Argo (symbols) and PATO (solid lines).

The results of test case 2.1 have demonstrated that the energy balance is correctly implemented. Indeed, when it is submitted to a convective heat flux, the surface temperature of the material is in good agreement with PATO.

4.2.3 Ablation test case 2.2: Convective heat flux with recession

Description and objectives

The test case 2.2 is similar to test case 2.1, but the recession of the material is taken into account. The ablation rate is read in the B' thermochemical table provided in the spreadsheet from the test case [44]. As a reminder (see Section 2.4), the ablation rate depends on the pressure at the wall p_w, the temperature at the wall T_w, and the dimensionless pyrolysis blowing rate B'_g.

The objective of this test is to verify the recession modeling. In particular, the abilities of the higher-order level-set method to model recession will be demonstrated. Moreover, the thermochemical table approach used to compute the ablation rate will also be verified.

Results

Fig. 4.4a shows the temperature field for TACOT submitted to a convective heat flux considering recession. The same numerical thermocouples as in test cases 1 and 2.1 are placed in the material. The vertical lines in Fig. 4.4a, mean that the recession is higher than the depth of the thermocouple, so it fails. Concerning the surface temperature, it can be observed that it is close to the results from PATO. Note that the surface temperature is lower than in the case where recession was not considered (see Fig. 4.1a). This shows

the advantage of using an ablative material as thermal protection system. The material degrades, but it allows to reduce the heat load. Enthalpy is carried away by the pyrolysis gas and the ablation products.

The pyrolysis and char mass blowing rates, the position of the pyrolysis and char zones, and the recession are shown in Fig. 4.4b. There are discrepancies with PATO for the pyrolysis blowing rate and the pyrolysis zone, but the reason is explained in Section 4.2.2. Concerning the char blowing and the char zone, the results are in good agreement with PATO.

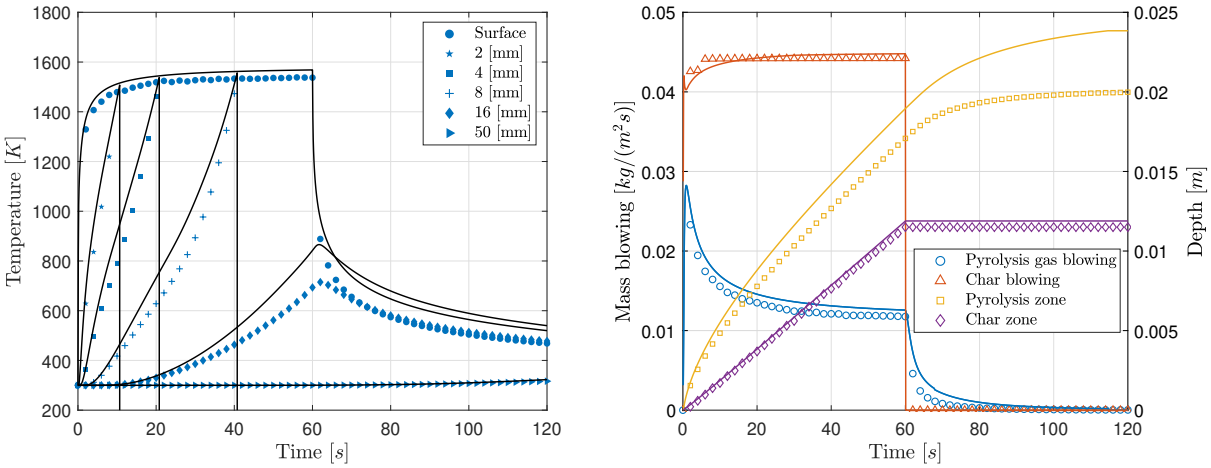

(a) Temperature field for TACOT

(b) Blowing rates, pyrolysis/char zone and recession

Fig. 4.4: In-depth thermal response for TACOT submitted to a convective heat flux with recession (Test case 2.2 [44]). Comparison between Argo (symbols) and PATO (solid lines).

The results shown in Fig. 4.4 prove that thanks to the level-set method, the recession is correctly modeled. Moreover, the results for the char blowing rate are close to PATO, which demonstrates that the method based on the B' thermochemical tables is correctly implemented.

4.3 Multi-dimensional test cases

The abilities of the material response code for one-dimensional cases have been successfully demonstrated in Section 4.2. The constitutive equations, the mass and energy balance, and the recession modeling are correctly implemented. The objective of this section is to verify if the code can treat multi-dimensional cases. For this purpose, the ablation test case 3 from Lachaud et al. [45] will be used. In this work, the two-dimensions axisymmetrical test cases (3.0 and 3.1) have been done. Due to limited computational resources, a three-dimensional test case has not been considered.

4.3.1 Ablation test case 3.0: 2D axisymmetrical without recession

Description and objectives

A sphere-cylinder sample of TACOT (see Fig. 4.5) is considered. The thermochemical properties of the material are different from test cases 1 and 2, and there are provided in the spreadsheet of the test case [45]. As shown in Fig. 4.5, the sphere curvature radius is equal to the diameter of the cylinder.

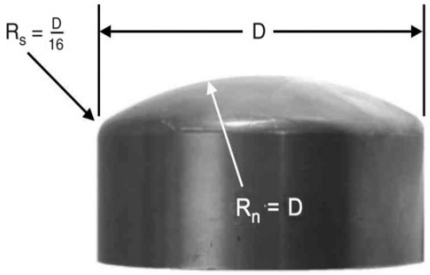

Fig. 4.5: Sphere-cylinder sample of TACOT modeled in the test case 3. Figure from [45].

As shown in Fig. 4.6, for the test cases 3.0 and 3.1, the geometry is simplified to an ellipse on top of a cylinder, and a 2D axisymmetrical projection of the sample is made. Note that in Fig. 4.6, the mesh depicted is the one realized in this work for the test case 3.0. The red points on the figure correspond to the different numerical thermocouples used in the test cases.

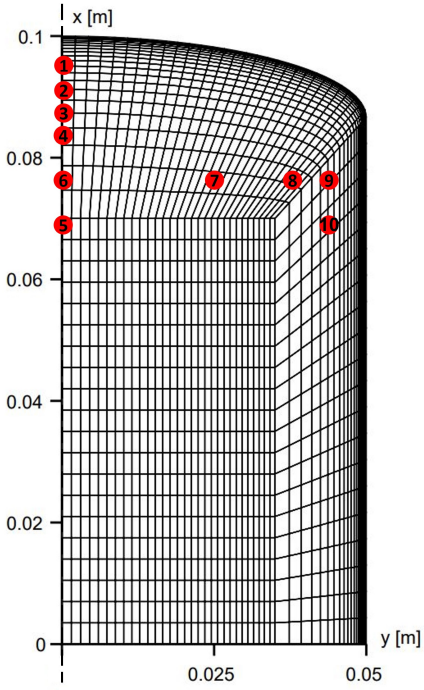

Fig. 4.6: 2D axisymmetrical mesh used for the test cases. The position of the different numerical thermocouples is given by the red points.

Concerning the boundary conditions, the material is submitted to a convective heat flux for $40[s]$ and then cooled down for $1[min]$ by radiative cooling. Concerning the initial conditions: $p_0 = 405.3[Pa]$ and $T_0 = 300[K]$. For the convective heat flux, typical arc-jet conditions have been used. The environment properties have been computed thanks to a CFD code [60]. The profiles for the heat-flux and the wall pressure are shown in Fig. 4.7, and the environment properties are given in Table 4.3.

The heat flux and the wall pressure depend on the arc length. For example, referring to Fig. 4.6, $p_w(0,t)$ and $p_w(11.17,t)$ corresponds to the wall pressure at the top $(x = 0.1, y = 0)$ and at the bottom $(x = 0, y = 0.5)$. Thanks to the profile given in Fig. 4.7, the heat flux at a particular arc length can be computed by multiplying $\rho_e u_e C_h(0)$ by $q_w/q_w(0)$. For the wall pressure, it is the same methodology.

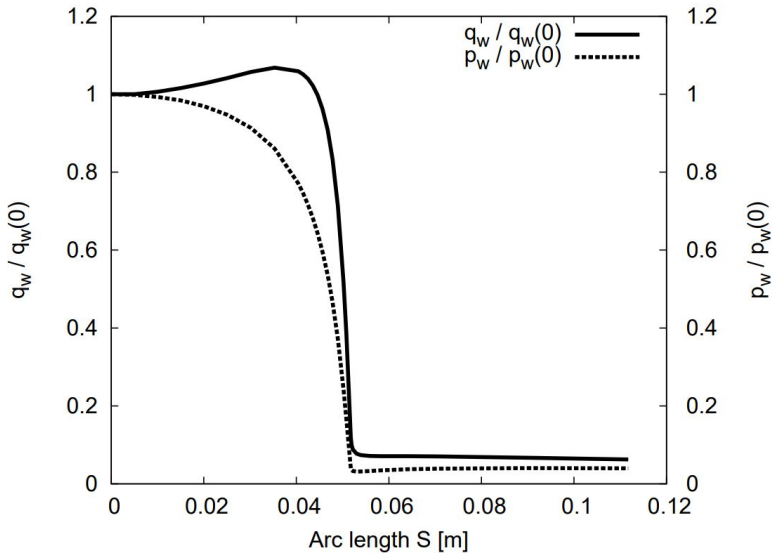

Fig. 4.7: Heat flux and pressure profiles. Figure from [45].

Table 4.3: Properties of the boundary layer for the test cases 3 [45].

Time $[s]$	$\rho_e u_e C_h(0)$ $[kg/(m^2 s)]$	$h_{0,e}$ $[J/kg]$	$p_w(0,t)$ $[Pa]$	$p_w(11.17,t)$ $[Pa]$
0	$0.1 \cdot 10^{-2}$	0	405.3	405.3
0.1	0.1	$2.5 \cdot 10^7$	10132.5	405.3
40	0.1	$2.5 \cdot 10^7$	10132.5	405.3
40.1	$0.1 \cdot 10^{-2}$	0	405.3	405.3
120	$0.1 \cdot 10^{-2}$	0	405.3	405.3

In test case 3.0, recession is not taken into account. The objective is to verify that the material response code can treat a multidimensional case.

Results

In this test case, due to limited computational resources and time constraints, only the heating phase (up to 40$[s]$) has been modeled and only C_6H_5OH is considered in the pyrolysis gas.

The results for the thermal response for TACOT submitted to a convective heat flux (considering typical arc-jet conditions) without recession (test case 3.0 [45]) are shown in Fig. 4.8. The temperature field at $t = 39[s]$ is depicted in Fig. 4.8a and the temperature along the outer surface is represented in Fig. 4.8b. The temperature is higher on the upper surface and reaches a peak of 2603$[K]$ at an arc length of 0.035$[m]$. The computed surface temperature is coherent, referring to the heat flux profile given in Fig. 4.7.

Fig. 4.8c and Fig. 4.8d shows the temperature field at the surface and at the numerical thermocouples 1 to 10. Due to the high convective heat flux, the surface temperature rises fast. The heat is transferred in-depth by thermal conduction, so the thermocouples temperature progressively increases. Note that at the thermocouple 5 (located at a depth of 3$[cm]$), the temperature reaches only 325$[K]$ at the end of the heating phase. It demonstrates that this material has good thermal protection abilities.

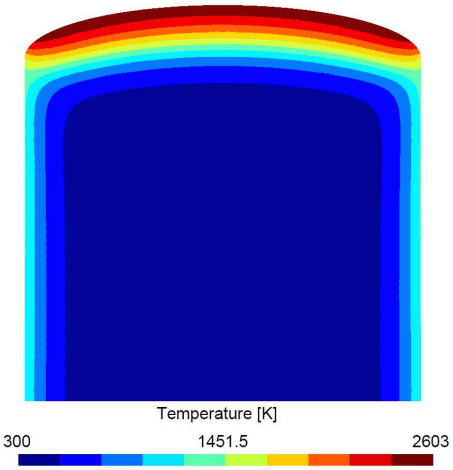

(a) Temperature field at $t = 39[s]$

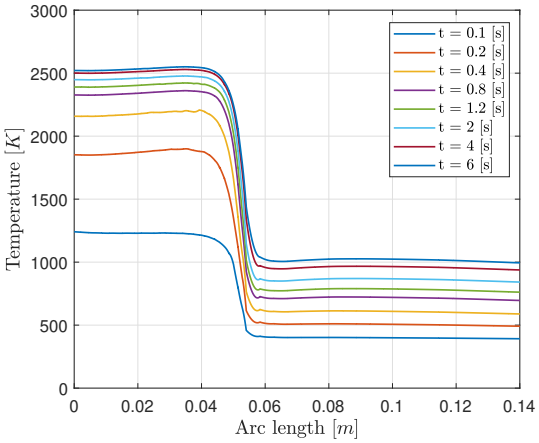

(b) Temperature along the outer surface

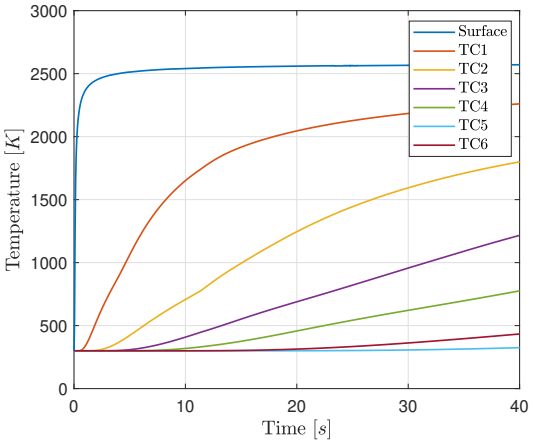

(c) Temperature field at the surface (top) and at the thermocouples 1 to 6 (see Fig. 4.6)

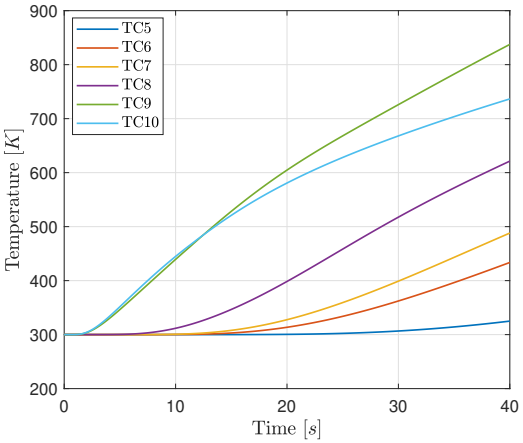

(d) Temperature field at the thermocouples 5 to 10 (see Fig. 4.6)

Fig. 4.8: In-depth thermal response for TACOT submitted to a convective heat flux (considering typical arc-jet conditions) without recession (test case 3.0 [45]).

Fig. 4.9a depicts the solid mass density at $t = 39[s]$. It can be observed that the mass density varies between $220[kg/m^3]$ (the density of charred TACOT) and $280[kg/m^3]$ (the density of virgin material). Along the boundary and particularly on the top (where the heat load is the most important), the material is carbonized, so the mass density is close to $220[kg/m^3]$. In-depth, the density is equal to $280[kg/m^3]$, which means that the material is virgin. Between the char and the virgin zone, the resin is pyrolyzing and partially charred, so the density is between 220 and $280[kg/m^3]$. The evolution of the degradation of the resin can also be observed in Fig. 4.9b. The mass density at the position of the different thermocouples progressively decreases because the resin is pyrolyzed and transformed into gas and char.

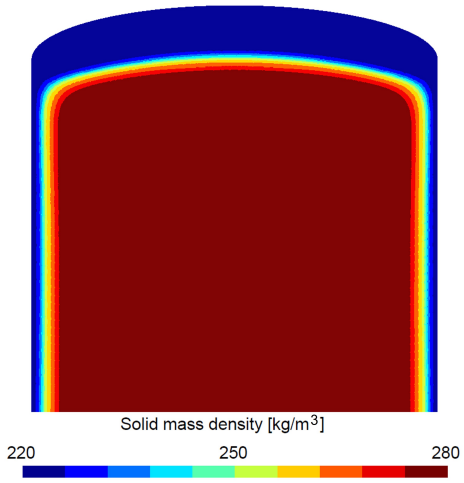

(a) Solid mass density at $t = 39[s]$

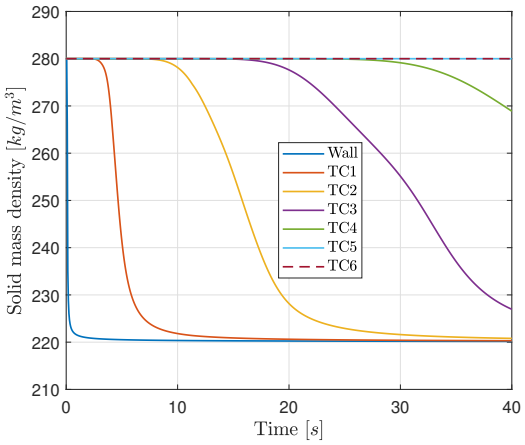

(b) Solid mass density at the surface and at the position of the thermocouples TC1-6

Fig. 4.9: Evolution of the solid mass density of TACOT submitted to a convective heat flux (test case 3.0 [45]). As a reminder, the mass density of pure char and virgin material are respectively $220[kg/m^3]$ and $280[kg/m^3]$.

The pyrolysis gas pressure field and velocity at $t = 39[s]$ are shown in Fig. 4.10a. The wall pressure corresponds to the one obtained with the pressure profiles (see Fig. 4.7). At the top (at an arc length of $0[m]$), it can be observed in Fig. 4.10a that the wall pressure is equal to $10132.5[Pa]$ which is the value given in Table 4.3. An interesting observation that can be made is that the pyrolysis gas percolates through the material and then leaves on the corners of the material. The zoom in Fig. 4.10b shows that the pyrolysis gas velocity is oriented in the direction of the pressure gradient. This makes sense referring to the momentum conservation equation described in Section 2.2.2. Indeed, the pyrolysis gas velocity (and its direction) is dependent on the pressure gradient.

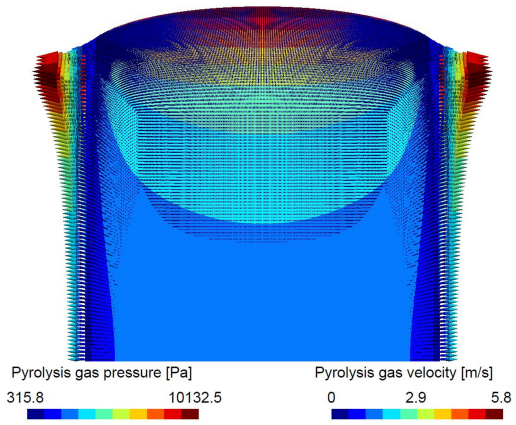

(a) Pyrolysis gas pressure field and velocity at $t = 39[s]$

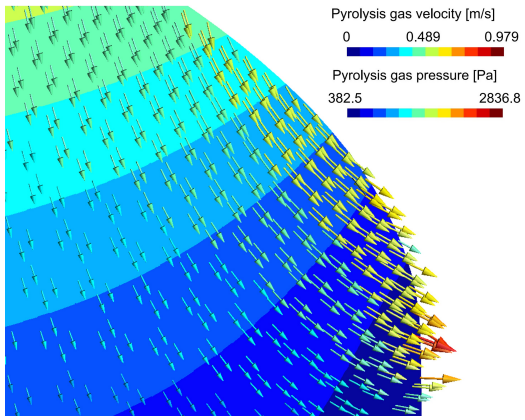

(b) Zoom on the pyrolysis gas pressure field and velocity at $t = 0.025[s]$

Fig. 4.10: Pyrolysis gas pressure field and velocity for the test case 3.0 [45].

The coherent results obtained for the temperature field, the evolution of the solid mass density, and the pyrolysis pressure and velocity demonstrate that the code can correctly treat 2D axisymmetrical problems. Note that the results obtained with state-of-the-art

codes were not accessible for comparison. Nevertheless, the results seem to be in good agreement with the results of Amaryllis depicted in the paper of the test case 3 [45].

4.3.2 Ablation test case 3.1: 2D axisymmetrical with recession

Description and objectives

The test case 3.1 is identical to test case 3.0 except that recession is taken into account. The constitutive equation and the implementation of the mass and energy balance have been verified for a 2D axisymmetrical case in Section 4.3.1. The objective now is to demonstrate the ability of the code to model recession using the level-set method considering a two-dimensions axisymmetrical geometry. To avoid redundancy, the focus for the results will be placed on the recession of the material. The idea is to prove and show that the interface moves due to the degradation of the material.

Results

For the test case 3.1, the simulation has been conducted only up to $10[s]$ due to time constraints and limited computational resources[7].

The temperature field at $t = 10[s]$ for the test case 3.1 is depicted in Fig. 4.11. Moreover, the recession of the surface is also represented in this figure. The initial surface geometry is represented in orange by the iso-0 level-set at $t = 0[s]$. The deformed surface due to recession is shown in green by the iso-0 level-set at $t = 10[s]$. It can be observed that the material degrades mostly in the zones where the temperature is high. In those zones, the resin is carbonized, and the remaining char and the carbon fibers are progressively ablated, which leads to recession (see Section 1.2.2).

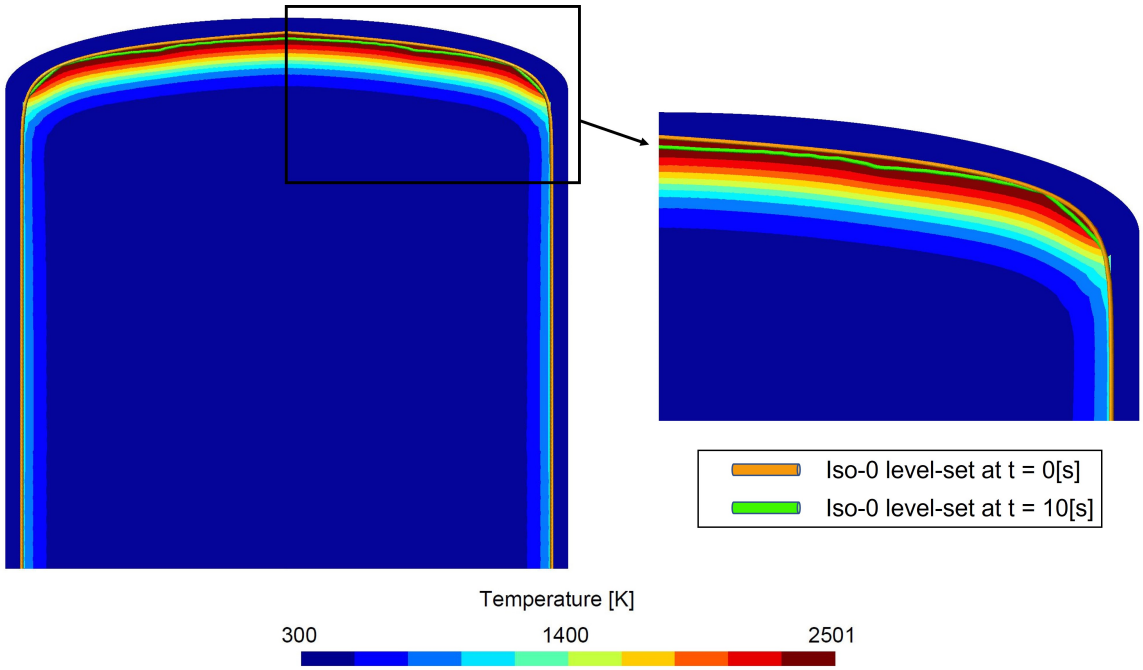

Fig. 4.11: Temperature field for TACOT submitted to a convective flux with recession at $t = 10[s]$ (test case 3.1 [45]). The deformation of the surface geometry due to recession is also depicted in the figure with the iso-0 level-set at $t = 0[s]$ and $t = 10[s]$.

[7] For the test case 3.1, it takes about one day to simulate $2[s]$ with a time step of $0.001[s]$

Fig. 4.12 shows the recession and the recession rate at the top of the material (at an arc length of $0[m]$, which is one of the crucial points where the recession is the highest). After $10[s]$, the recession reaches $1.1[mm]$. Concerning the recession rate, it can be observed that it is relatively constant.

Fig. 4.13 compares the temperature at the surface and at the thermocouple 1 to 4 (see Fig. 4.6) for the test case 3.0 without recession (dotted lines) and the test case 3.1 (colored solid lines). At the surface, the temperature is slightly lower when recession is considered. This can be explained by the fact that the surface (which is at high temperature) recedes. Moreover, the ablation product carries enthalpy out of the material (see Section 2.3.2). In-depth, for instance, at the thermocouple 1, the temperature is higher when there is recession. This is simply because, due to the surface recession, the thermocouple is closer to the surface, and thus its temperature is higher.

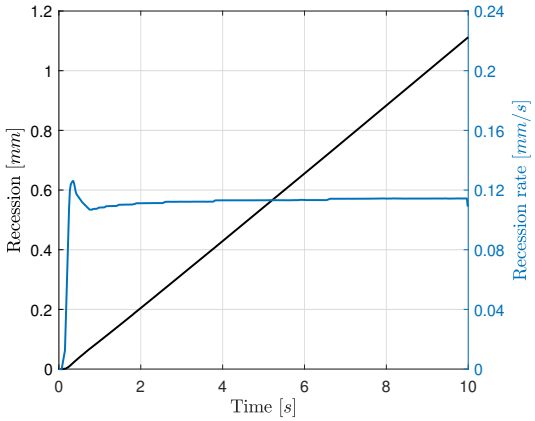

Fig. 4.12: Recession and recession rate of the surface of the material for the test case 3.1 [45].

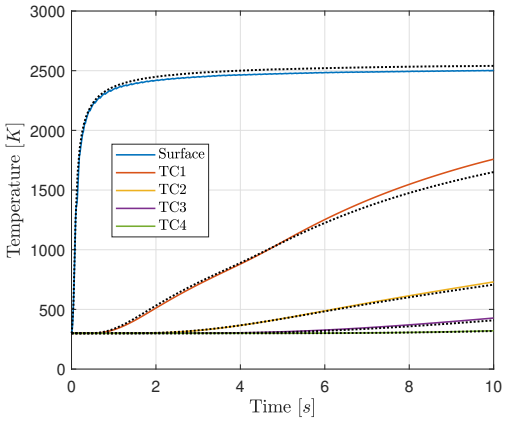

Fig. 4.13: Comparison between the temperature field obtained for the test case 3.0 (doted black lines) and 3.1 (colored lines).

The results obtained for test case 3.1 show the ability of the code to model recession in a two-dimensions axisymmetrical problem. The level-set method implemented in Argo allows to capture the deformation of the surface and deal with the moving boundary.

4.4 Conclusion

The results presented in this section demonstrate that the material response code can model the in-depth thermal response and the recession of ablative materials. The constitutive equations from Argo, the implementation of the surface mass and energy balance, and the recession modeling have been verified thanks to the test cases from Lachaud et al. [33, 44, 45]. The Argo results are in good agreement with results from state-of-the-art codes such as PATO [28]. Discrepancies in the in-depth temperature have been observed, but this is because the model used in Argo and PATO is not the same. Therefore, when several species are considered in the pyrolysis gas, the thermal and transport properties differ, leading to discrepancies in the thermal response. The results obtained with the test case 3 [45] are interesting because they show the ability of the code to treat multi-dimensional ablation problems. The different figures presented in Section 4.3 also allow to better understand and visualize the response of an ablative material submitted to typical arc-jet conditions.

5 Conclusion

5.1 Achievements

In the present work, a material response code capable of modeling the in-depth thermal response of an ablative material submitted to a high enthalpy flow has been developed. The numerical tool can treat multi-dimensional ablation problems while accounting for the recession of the material. The code is based on Argo, a multi-physics platform with a dedicated module for ablation problems. The main advantage of this numerical tool is that it is based on a high order discontinuous Galerkin method, which provides accuracy for unstructured mesh and computational efficiency.

A material response solver based on a strong coupling approach was already implemented in Argo by Schrooyen [6]. This high fidelity solver can accurately capture the gas-surface interactions, but it is computationally expensive. Therefore, in this work, a new boundary condition was added in Argo to simplify the approach and consider a material solver only. A surface mass and energy have been implemented to model the heat and mass flux at the solid-gas interface. The degradation phenomena of the ablative material (pyrolysis and ablation) are both accounted for. The ablation rate is obtained thanks to B' thermochemical tables, and the immersed level-set method implemented in Argo is used to model the recession of the material and to deal with the moving boundary problem.

The results obtained for the test cases from Lachaud et al. [33, 44, 45] have proven the ability of the material response code to model the in-depth thermal response of ablative materials. If the same material and pyrolysis gas properties are considered, the Argo results are in good agreement with the results obtained with state-of-the-art codes such as PATO. The use of B' thermochemical tables to compute the ablation rate and the abilities of the level-set method to model recession have been successfully demonstrated. The various test cases realized during this work also allowed to deeply understand the phenomena involved in the degradation of an ablative material submitted to typical atmospheric entry conditions. Moreover, the test case 3 showed that the material response code can treat multi-dimensional ablation problems. In particular, the results obtained for the two-dimensions axisymmetrical test cases prove that the immersed level-set method from Argo can deal with complex interface geometry and model recession accurately.

This work has demonstrated that a solver based on Argo and a material approach is promising. The satisfactory results obtained for the in-depth thermal response and the recession have proven that this approach is worthy to investigate further.

5.2 Perspectives

The implementation of the surface mass and energy balance, and the use of thermochemical tables is a first step in the development of a multi-dimensional material solver based on Argo. Some improvements can be made to reach a higher fidelity level and optimize the material response code.

First, in this work, the homogeneous reactions between the species in the pyrolysis gas and in the boundary layer have not been considered and investigated. Note that the homogeneous reactions are already implemented in Argo, but they have not been taken into account due to time and computational constraints. It could be interesting in a future

work to consider those reactions and compare the changes in the results for the different test cases.

Other improvements can be added to the model to reach a higher fidelity. For instance, the anisotropy of the material could be taken into account by implementing an orthotropic model for the thermal conductivity and/or the permeability. Moreover, some complex phenomena such as radiative heating or spallation (mechanical ablation) could be considered.

The presented material response code provides satisfactory results, but it should be further verified with other test cases. The code has been tested with one-dimensional and two-dimensions axisymmetrical cases. A three-dimensional problem has not been investigated because it is computationally expensive. The code implemented in this work could certainly be optimized to reduce the computational cost (for example, by optimizing: the memory access, the lecture of the B' thermochemical tables, etc.). With an optimized code and better computational resources, three-dimensional test cases could be performed. An interesting perspective could be to observe the ability of the level-set method to deal with a complex three-dimensional geometry.

Moreover, the benefits of the code in terms of computational efficiency compared to the strong coupling approach should also be investigated in a future work. Indeed, one of the objectives of developing a material approach was to reduce the computational cost.

In conclusion, the multi-dimensional material response code developed in this work consists a first base for further investigations. The material solver approach provided satisfactory results, but the code can be optimized and improved to achieve higher fidelity and better computational efficiency.

Bibliography

[1] S. L. Post. Space Shuttle Case Studies: Challenger and Columbia. In *2014 ASEE Annual Conference & Exposition*, Indianapolis, Indiana. ASEE Conferences, June 2014.

[2] NASA. Aerothermodynamics Course, Lecture #1 Stagnation Point Heating.

[3] R. Harris, M. Stewart, and W. Koenig. Thermal Protection Systems Technology Transfer from Apollo and Space Shuttle to the Orion Program. In *2018 AIAA SPACE and Astronautics Forum and Exposition*. American Institute of Aeronautics and Astronautics, 2018.

[4] M. Stackpoole, S. Sepka, I. Cozmuta, and D. Kontinos. Post-Flight Evaluation of Stardust Sample Return Capsule Forebody Heatshield Material. In *46th AIAA Aerospace Sciences Meeting and Exhibit*, Reno, Nevada. American Institute of Aeronautics and Astronautics, January 2008.

[5] M. B. Kirkham. Chapter 3 - Structure and Properties of Water. In M. B. Kirkham, editor, *Principles of Soil and Plant Water Relations (Second Edition)*, pages 27–40. Academic Press, Boston, January 2014.

[6] P. Schrooyen. *Numerical simulation of aerothermal flows through ablative thermal protection systems*. PhD thesis, Université catholique de Louvain, Louvain-la-Neuve, 2015.

[7] D. Potter. *Modelling of radiating shock layers for atmospheric entry at Earth and Mars*. PhD thesis, University of Queensland, 2011.

[8] J. Lachaud, T. E. Magin, I. Cozmuta, and N. N. Mansour. A Short Review of Ablative-Material Response Models and Simulation Tools. In Bruges, May 2011.

[9] C. O. Johnston, P. A. Gnoffo, and K. Sutton. Influence of Ablation on Radiative Heating for Earth Entry. *Journal of Spacecraft and Rockets*, 46(3):481–491, 2009.

[10] D. Bianchi. *Modeling of ablation phenomena in space applications*. PhD thesis, Universita degli Studi di Roma, 2007.

[11] J. W Lawson, M. M. Stackpoole, E. Corp, and V. Shklover. Examination of Scanning Electron Microscope and Computed Tomography Images of PICA:15, 2010.

[12] J. Lachaud, I. Cozmuta, and N. N. Mansour. Multiscale Approach to Ablation Modeling of Phenolic Impregnated Carbon Ablators. *Journal of Spacecraft and Rockets*, 47(6):910–921, 2010.

[13] F. Buffenoir, T. Pichon, and R. Barreteau. IXV Thermal Protection System Post-Flight Preliminary analysis, 2017.

[14] T. Greicius. NASA's Stardust Sample Return was 10 Years Ago Today, January 2016.

[15] B. Chanetz, J. Délery, P. Gilliéron, P. Gnemmi, E. R. Gowree, and P. Perrier. Hypersonic Wind Tunnels. In *Experimental Aerodynamics: An Introductory Guide*, Springer Tracts in Mechanical Engineering, pages 135–164. Springer International Publishing, 2020.

[16] P. Thakre and V. Yang. Chemical Erosion of Carbon–Carbon/Graphite Nozzles in Solid-Propellant Rocket Motors. *Journal of Propulsion and Power*, 24:822–833, July 2008.

[17] D. Bianchi, A. Turchi, F. Nasuti, and M. Onofri. Chemical Erosion of Carbon-Phenolic Rocket Nozzles with Finite-Rate Surface Chemistry. *Journal of Propulsion and Power*, 29(5):1220–1230, 2013.

[18] Y. Chen and F. Milos. Navier-Stokes Solutions with Finite Rate Ablation for Planetary Mission Earth Reentries, 2005.

[19] D. Bianchi, F. Nasuti, and E. Martelli. Navier–Stokes Simulations of Hypersonic Flows with Coupled Graphite Ablation. *Journal of Spacecraft and Rockets*, 47:554–562, July 2010.

[20] B. Hassan, D. Kuntz, and D. L. Potter. Coupled Fluid/Thermal Prediction of Ablating Hypersonic Vehicles. In 1998.

[21] Y. Chen and T. Gokcen. Loosely Coupled Simulation for Two-Dimensional Ablation and Shape Change. 47, June 2013.

[22] D. Bianchi, A. Turchi, F. Nasuti, and M. Onofri. Coupled CFD Analysis of Thermochemical Erosion and Unsteady Heat Conduction in Solid Rocket Nozzles. In July 2012.

[23] Y. Chen and T. Gokcen. Implicit Coupling Approach for Simulation of Charring Carbon Ablators. In San Diego, CA, June 2013.

[24] Y. Chen, F. Milos, and D. Rasky. Fully Implicit Ablation and Thermal Response Program for Spacecraft Heatshield Analysis, February 1997.

[25] R. Gosse and G. Candler. Ablation Modeling of Electro-Magnetic Launched Projectile for Access to Space. In *45th AIAA Aerospace Sciences Meeting and Exhibit*, Aerospace Sciences Meetings. American Institute of Aeronautics and Astronautics, January 2007.

[26] A. Martin. Volume averaged modeling of the oxidation of porous carbon fiber material. In *44th AIAA Thermophysics Conference*, Fluid Dynamics and Co-located Conferences. American Institute of Aeronautics and Astronautics, June 2013.

[27] E. P. Bartlett, R. M. Kendall, C. B. Moyer, and R. A. Rindal. An analysis of the coupled chemically reacting boundary layer and charring ablator. part 1: Summary report. Technical report, June 1968.

[28] J. Lachaud and N. N. Mansour. Porous-Material Analysis Toolbox Based on OpenFOAM and Applications. *Journal of Thermophysics and Heat Transfer*, 28(2):191–202, 2014.

[29] R. Davuluri and A. Martin. Numerical Study of Spallation Phenomenon in an Arc-Jet Environment. *Proceedings of the 11th AIAA/ASME Joint Thermophysics and Heat Transfer Conference*:1–16, June 2014.

[30] G. Pinaud and T. van Eekelen. A numerical comparison of high-and low fidelity radiation models for conduction-radiation coupling in (charring) ablators. *7th European Workshop on Thermal Protection Systems and Hot Structures*, 2013.

[31] F. S. Milos and Y.-K. Chen. Two-Dimensional Ablation, Thermal Response, and Sizing Program for Pyrolyzing Ablators. *Journal of Spacecraft and Rockets*, 46(6):1089–1099, November 2009.

[32] Y.-K. Chen, F. Milos, and T. Gokcen. Validation of a Three-Dimensional Ablation and Thermal Response Simulation Code. In *10th AIAA/ASME Joint Thermophysics and Heat Transfer Conference*, Fluid Dynamics and Co-located Conferences. American Institute of Aeronautics and Astronautics, June 2010.

[33] J. Lachaud, A. Martin, I. Cozmuta, and B. Laub. Ablation workshop test case. *4th Ablation Workshop*, March 2011.

[34] Y.-K. Chen and F. S. Milos. Ablation and Thermal Response Program for Spacecraft Heatshield Analysis. *Journal of Spacecraft and Rockets*, 36(3):475–483, 1999.

[35] Y.-K. Chen and F. S. Milos. Two-Dimensional Implicit Thermal Response and Ablation Program for Charring Materials. *Journal of Spacecraft and Rockets*, 38(4):473–481, July 2001.

[36] Y.-K. Chen and F. Milos. Three-Dimensional Ablation and Thermal Response Simulation System. In *38th AIAA Thermophysics Conference*, Fluid Dynamics and Co-located Conferences. American Institute of Aeronautics and Astronautics, June 2005.

[37] Y.-K. Chen and Frank S. Milos. Multidimensional Finite Volume Fully Implicit Ablation and Thermal Response Code. *Journal of Spacecraft and Rockets*, 55(4):914–927, July 2018.

[38] Y.-K. Chen and F. S. Milos. Multidimensional Effects on Heatshield Thermal Response for the Orion Crew Module. In *39th AIAA Thermophysics Conference*, Fluid Dynamics and Co-located Conferences. American Institute of Aeronautics and Astronautics, June 2007.

[39] Yih-Kanq Chen and Frank S. Milos. Effects of Nonequilibrium Chemistry and Darcy—Forchheimer Pyrolysis Flow for Charring Ablator. *Journal of Spacecraft and Rockets*, 50(2):256–269, 2013.

[40] B. Gorissen. 1d code for discontinuous galerkin methods. Cenaero, Private Communication.

[41] P. Schrooyen, K. Hillewaert, T. Magin, and P. Chatelain. Discontinuous Galerkin discretization coupled with sharp interface method for ablative materials. In June 2013.

[42] K. Sutton and P. Gnoffo. Multi-component diffusion with application to computational aerothermodynamics. In *7th AIAA/ASME Joint Thermophysics and Heat Transfer Conference*. American Institute of Aeronautics and Astronautics, June 1998.

[43] H. E. Goldstein. Kinetics of Nylon and Phenolic Pyrolysis. Technical report, Lockheed Missiles and Space Co Inc Sunnyvale CA, October 1965.

[44] J. Lachaud, A. Martin, I. Cozmuta, and B. Laub. Ablation test-case series #2. In March 2012.

[45] T. van Eekelen, J. Lachaud, A. Martin, and I. Cozmuta. Ablation test-case series #3. *6th Ablation Workshop*, February 2014.

[46] S. Ganesan and D. R. Poirier. Conservation of mass and momentum for the flow of interdendritic liquid during solidification. *Metallurgical Transactions B*, 21(1):173, February 1990.

[47] S. Whitaker. The Method of Volume Averaging. *Theory and Applications of Transport in Porous Media*, 1999.

[48] N. Puiroux, M. Prat, and M. Quintard. Non-equilibrium theories for macroscale heat transfer: ablative composite layer systems. *International Journal of Thermal Sciences*, 43(6):541–554, June 2004.

[49] J. A. Dec, R. D. Braun, and B. Laub. Ablative Thermal Response Analysis Using the Finite Element Method. *Journal of Thermophysics and Heat Transfer*, 26(2):201–212, 2012.

[50] C. B. Moyer and R. A. Rindal. An analysis of the coupled chemically reacting boundary layer and charring ablator. Part 2 - Finite difference solution for the in-depth response of charring materials considering surface chemical and energy balances. Technical report, June 1968.

[51] F. S. Milos and D. J. Rasky. Review of numerical procedures for computational surface thermochemistry. *Journal of Thermophysics and Heat Transfer*, 8(1):24–34, January 1994.

[52] R. M. Kendall and R. A. Rindal. An analysis of the coupled chemically reacting boundary layer and charring ablator. part 5: A general approach to the thermochemical solution of mixed equilibrium-nonequilibrium, homogeneous or heterogeneous systems. Technical report, June 1968.

[53] E. P. Bartlett, R. M. Kendall, and R. A. Rindal. Thermochemical ablation. Technical report, September 1965.

[54] J.J. Brogan. A numerical method of solution for heat conduction in composite slabs with a receding surface. Technical report LMSD 288204, Lockheed Aircraft Corp, April 1960.

[55] C. W Hirt and B. D Nichols. Volume of fluid (VOF) method for the dynamics of free boundaries. *Journal of Computational Physics*, 39(1):201–225, January 1981.

[56] H. Liu, Y. Tian, H. Zong, Q. Ma, M. Y. Wang, and L. Zhang. Fully parallel level set method for large-scale structural topology optimization. *Computers & Structures*, 221:13–27, September 2019.

[57] F. Chen and H. Hagen. A Survey of Interface Tracking Methods in Multi-phase Fluid Visualization. In *Visualization of Large and Unstructured Data Sets - Applications in Geospatial Planning, Modeling and Engineering (IRTG 1131 Workshop)*, volume 19, pages 11–19. Schloss Dagstuhl–Leibniz-Zentrum fuer Informatik, 2011.

[58] W. J. Rider and D. B. Kothe. Reconstructing Volume Tracking. *Journal of Computational Physics*, 141(2):112–152, April 1998.

[59] D. Henneaux, P. Schrooyen, L. Arbaoui, P. Chatelain, and T. Magin. A High-Order Level-Set Method Coupled with an Extended Discontinuous Galerkin Method for Simulating Moving Interface Problems. In August 2021.

[60] A. Martin, L. C. Scalabrin, and I. D. Boyd. High performance modeling of atmospheric re-entry vehicles. *Journal of Physics: Conference Series*, 341:012002, February 2012.

[61] J. Lachaud, T. van Eekelen, J. B. Scoggins, T. E. Magin, and N. N. Mansour. Detailed chemical equilibrium model for porous ablative materials. en. *International Journal of Heat and Mass Transfer*, 90:1034–1045, November 2015.

UNIVERSITÉ CATHOLIQUE DE LOUVAIN
École polytechnique de Louvain
Rue Archimède, 1 bte L6.11.01, 1348 Louvain-la-Neuve, Belgique | **www.uclouvain.be/epl**